



# A comparative study of irradiation response in amorphous TaTiWVCr refractory high entropy alloy with the counterpart of tungsten films

Guo Pu<sup>a</sup>, Sen Sun<sup>b</sup>, Sishu Wang<sup>c</sup>, Lin Gan<sup>a</sup>, Sheng Chen<sup>a</sup>, Zongbiao Ye<sup>a</sup>, Zhangyi Huang<sup>d</sup>, Jiaochun Zheng<sup>d</sup>, Zhijun Wang<sup>d</sup>, Chi Yang<sup>d</sup>, Liwei Lin<sup>a</sup>, Bo Liu<sup>a</sup>, Kun Zhang<sup>a</sup>, Yihan Wang<sup>a,\*</sup>

<sup>a</sup> Key Laboratory of Radiation Physics and Technology of Ministry of Education, Institute of Nuclear Science and Technology, Sichuan University, Chengdu, 610064, PR China

<sup>b</sup> Nuclear Waste Disposal Engineering Research Center, School of Mathematics and Physics, Mianyang Teachers' College, Mianyang, 621000, PR China

<sup>c</sup> Institute of Atomic and Molecular Physics, Sichuan University, Chengdu, 610064, PR China

<sup>d</sup> Institute for Advanced Study, Chengdu University, Chengdu, 610106, PR China

## ARTICLE INFO

### Keywords:

Refractory high entropy alloy  
Irradiation-induced crystallization  
Electronic energy loss  
Phase structure stability  
Short-range segregation  
Irradiation swelling

## ABSTRACT

In this work, tungsten-containing TaTiWVCr refractory high entropy alloy (RHEA) and tungsten (W) films with amorphous structures were irradiated by a 60 keV helium (He) ion beam platform, the fluences were ranging from  $1 \times 10^{16} \text{ cm}^{-2}$  to  $2 \times 10^{17} \text{ cm}^{-2}$ . Results showed that the crystallization phenomenon in RHEA initially happened at fluence of  $5 \times 10^{16} \text{ cm}^{-2}$ . Meanwhile, the obvious crystallization in W films was induced at the highest fluence of  $2 \times 10^{17} \text{ cm}^{-2}$ . This indicated that the crystallization and the grain growth in TaTiWVCr RHEA amorphous films were more easily occurred than that of W films when exposed to the same He<sup>+</sup> environment. The prominent electronic stopping power and He<sup>+</sup> energy deposition induced electron excitation played vital role in producing inelastic thermal-spikes via electron-phonon coupling, which was contributed to the crystallization kinetic energy and the overall grain growth in irradiated regions. The phase structure of RHEA film kept stable up to the highest fluence of  $2 \times 10^{17} \text{ cm}^{-2}$ , even though the alloy elements demonstrated local short-range segregation due to the diffusion-driven crystallization and the formation of highly-pressurized bubbles in the irradiated RHEA. In contrast to the W, smaller-sized bubbles and less dislocations were mainly distributed in the irradiated region of RHEA due to its naturally special high entropy effect and high lattice distortion. Besides, the results of irradiation-induced superficial morphology and volume swelling revealed that the RHEA exhibited more excellent swelling resistance than that of W. This study will potentially provided a useful indicator of RHEA with self-healing stability to resist irradiation and promote the development of state-of-the-art plasma-facing materials for the future nuclear fusion.

## 1. Introduction

In the international thermonuclear experimental reactor (ITER), metal tungsten (W) has been regarded as a leading material used for the critical components of nuclear fusion, such as the divertors or the plasma-facing materials (PFMs), which must be confronted with high temperature environment ( $\geq 1000 \text{ K}$ ) for quite long durations ( $\geq 10^7 \text{ s}$ ). Meanwhile, the potential PFM candidates exhibit excellent ability to resist failure or extensive damage exposed to high-flux (fluxes  $> 10^{24} \text{ m}^{-2} \text{ s}^{-1}$ ) hydrogen isotopes (deuterium and tritium) plasma and intense energy helium (He) ion and neutron irradiation [1,2]. Abundant contributory efforts have been devoted to understand the interaction

between the He atoms and the pure W material from the perspective of experiments and simulations [3–5]. Nevertheless, the disadvantages of W materials, such as low fracture toughness coupled with adverse resistance to high heat-loading and energetic ion irradiation, severely constrain the widened operating temperature window and the enhanced irradiation damage (dpa) [5]. Therefore, exploring innovative candidate materials are required to have advantageous properties including low activation, high melting temperature, stable thermomechanical properties, low sputter etching, etc [3–5]. The proposition and design of novel high-entropy alloys inspired the development of W-containing refractory high entropy alloys (RHEAs) [6–10], such as, CrMoVW [11], TiNbMoTaW [12], HfNbTaTiZrW [13], etc. Except for the special

\* Corresponding author.

E-mail address: [yhwang027@scu.edu.cn](mailto:yhwang027@scu.edu.cn) (Y. Wang).

solid-solution structure, high temperature resistance and excellent mechanical properties [14,15], a small amount of literature also revealed that W-containing RHEAs or W-based RHEAs exhibit outstanding irradiation tolerance due to its high entropy effect and sluggish diffusion capacity [16–20]. Based on the fundamental results of previous researches, the W-containing RHEAs are proposed as a family of candidate materials used for PFM in the future advanced fusion reactors [21].

At present, many investigations have mainly explored the influence of the composition in tungsten-based RHEA on the phase structure as well as the ion irradiation induced micro-structure modification [16–21]. Zhang et al. [17] and Waseem et al. [18] found an unambiguous relationship between the element composition and phase-structure by reason of the enhanced lattice strain and the free-energy in W-containing RHEAs. The significant discrepancy of formation enthalpy between these metal elements in the  $TixW_{1-x}TaVCr(x = 0, 0.04, 0.07)$  RHEAs can result in the multi-phase precipitation, such as binary ( $Ta_2V$ ) or ternary ( $Ti-Cr-V$ ) alloys. Moreover, a dependence of irradiation resistance on the W contents was investigated in the  $W_x(TaVCrTi)_y$  RHEAs, revealing that the W-containing RHEAs exhibit excellent irradiation resistance and self-healing due to the existence of amorphization-recrystallization process [19]. Similarly, El-atwani et al. [20] disclosed that  $W38Ta36Cr15V11$  RHEA demonstrated outstanding irradiation resistance under the in-situ and ex-situ  $Kr^{2+}$  (1 MeV) irradiation at room temperature and 1073 K, respectively, while the Cr-rich and V-rich phase was also induced on account of the chemical ordering between the transition metals leads to a strong solute segregation of Cr and V. The diffusion-driven phase decomposition in  $V2.5Cr1.2WMoCo0.04$  RHEA with a single-phase structure was also detected owing to the enhanced defect density and the continual evolution of new defects [21]. According to the above studies, the irradiation-induced precipitations may potentially influence the structural stability and defect evolution. It is essential to explore the irradiation tolerance and phase stability of W-containing RHEA by investigating the interactions between the alloy atom and the He ions.

From the perspective of tailoring irradiation tolerance, the HEAs containing nano-grains demonstrated promising irradiation tolerance due to their intrinsically high-density grain boundaries (GBs) [22,23], which can act as effective defect sinks to attract He atoms or irradiation-induced point defects, and accordingly eliminate any kind of irradiation damage. To improve the irradiation tolerance of HEA, both heterogeneous and homogeneous interfaces between the multilayers were also designed to suppress He bubble growth [24–26]. Besides, homologous research reported that Zr-based amorphous alloy maintained amorphous state to resist high-energy (500 keV)  $He^{2+}$  irradiation [27]. Zhang et al. [28] reported that the irradiation-induced nano-grains were precipitated in amorphous multi-component alloy because of the irradiation-induced interstitials coalesces and precipitations. The other studies [29,30] synchronously revealed that the crystallization is ascribed to irradiation-driven self-migration and local heating in amorphous alloy which irradiated by energetic heavy-ions. Up to now, less work has been done to explore the low energy (<100 keV)  $He^+$  induced crystallization and the defect distributions in W-containing RHEAs with amorphous structures. As opposed to the energetic heavy-ion irradiation, it is a noteworthy topic that whether the significant discrepancy of energy loss produced by low energy  $He^+$  irradiation will affect the structural transformation from amorphous to crystallization. Those high-density GBs induced by irradiation can be regarded as an effective defect sink to annihilate the point-defects. As well known, the He bubble accumulation in alloys could significantly increase bubble pressure and lattice stress, leading to the solute segregation and promoting the formation of secondary phase ultimately [25,26]. Therefore, the inhibition of bubble growth and the enhancement of phase stability of RHEAs will be realized to improve its irradiation tolerance by controlling the bubble growth and its distribution due to the prominent contribution of increased nano-scale GBs in amorphous matrix. In contrast to the pure W materials, the complex defect energy landscape

exists in the W-containing RHEAs and because of its composition complexity and severe lattice distortion [31]. Such chemical heterogeneity in RHEAs also results in distinct energy landscapes that modify the mobility ability for those irradiation generated defects [32]. At present, the influences of same  $He^+$  irradiation on the structural modification and the irradiation response of RHEA were neglected in comparison with that of W materials. The mechanisms of irradiation resistance and the physical process of the interaction between the irradiated ions and the materials are needed to be further explored to reveal the advantages of irradiation tolerance for the two kinds of PFM candidates.

In this work, W-containing  $TaTiWVCr$  RHEA and W films with amorphous structures were obtained by radio frequency (RF) magnetron sputtering. These as-deposited films were irradiated by 60 keV  $He^+$  at the fluence ranging from  $1 \times 10^{16} \text{ cm}^{-2}$  to  $2 \times 10^{17} \text{ cm}^{-2}$  to explore the irradiation damage and volume swelling. Based on the results, the irradiation-enhanced crystallization phenomena in RHEA were disclosed at fluence of  $5 \times 10^{16} \text{ cm}^{-2}$  and the phase structure remained stable even though the fluence increased to  $2 \times 10^{17} \text{ cm}^{-2}$ . By contrast, the dramatic crystallization in W film was induced at the highest fluence of  $2 \times 10^{17} \text{ cm}^{-2}$ . The stopping power and  $He^+$  energy deposition were also simulated to explain the mechanisms of irradiation-induced crystallization during ion irradiation. At the highest fluence, in comparison with the W, the smaller-sized bubbles and the less dislocations were mainly produced in the irradiated region of RHEA due to its naturally high entropy effect and high lattice distortion. Meanwhile, the morphology characteristic and the volume swelling between RHEA and W films were also contrasted by the systematic investigations to explore their irradiation tolerance and swelling resistance. This comparative study can not only reveal the mechanisms of irradiation-enhanced crystallization, but also provide a fundamental understanding about the self-healing behavior in these two kinds of amorphous materials.

## 2. Experimental details

The  $TaTiWVCr$  RHEA and W films with amorphous structures were deposited by RF magnetic sputtering facility (CKBRY-420) at ambient temperature. One 60° inclination angle and a perpendicular distance of 100 mm were fixed in sputtering apparatus to adjust the film deposition (as the illustration shown in Fig. 1(a)). Before deposition, the substrates of silicon (Si) wafers were ultrasonically cleaned by acetone, alcohol and deionized water, respectively. The chamber was evacuated to a background pressure lower than  $7 \times 10^{-5} \text{ Pa}$  to reduce air pollution, and high-purity Ar (99.999%) with flow rate of 15 sccm provided a working pressure of 0.3 Pa.  $TaTiWVCr$  RHEA films were sputtered from the nominal composition  $TaTiWVCr$  (equimolar ratio) multi-component target ( $\varphi 55 \times 5 \text{ mm}$ ), which was manufactured by powder metallurgy technology with high purity (>99.99%, weight percent) raw materials of tantalum, titanium, tungsten, vanadium and chromium powders. The deposition power was adjusted at 150 W for the RHEA films to obtain a reasonable deposition rate of  $14.6 \text{ nm min}^{-1}$ . To keep the composition uniformity of these films, the sample holder rotated at a speed of 25 rpm during the deposition. Besides, the W films with similar amorphous structures were also prepared at the power of 110 W to carry out comparative study under the same  $He^+$  irradiation. Afterwards, these as-deposited films were irradiated by Kaufman injection machine with 60 keV  $He^+$  ion-beam system, the simplified apparatus was illustrated in Fig. 1(b). During the irradiation,  $He^+$  flux was fixed at  $5.56 \times 10^{13} \text{ cm}^{-2} \text{ s}^{-1}$ , and the  $He^+$  fluences were ranging from  $1 \times 10^{16} \text{ cm}^{-2}$  to  $2 \times 10^{17} \text{ cm}^{-2}$ . The partial region of samples was masked by tin foil to obtain unirradiated region and irradiated region, as shown in Fig. 1(c). The as-deposited  $TaTiWVCr$  RHEA and W films were fixed on a water-cooled holder to keep room temperature in chamber during  $He^+$  bombardment samples.

Displacement per atom (dpa) due to the exposure of  $TaTiWVCr$  RHEA and W films to 60 keV  $He^+$  at different fluences was simulated by the Stopping and Range of Ions in Matter (SRIM) code [33]. All

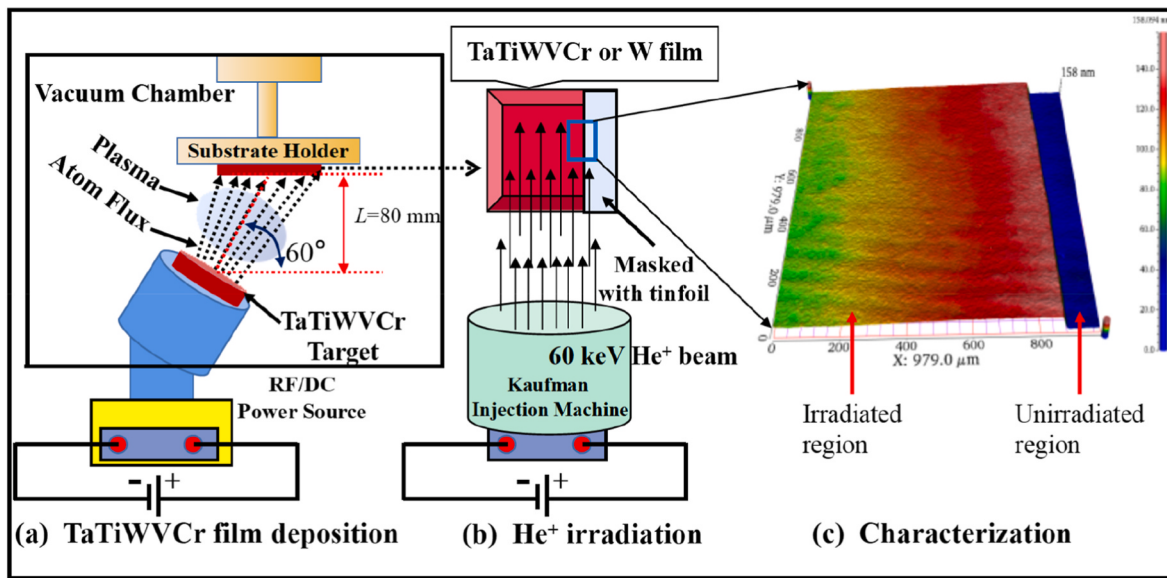


**Fig. 1.** (a) The detailed deposition apparatus of TaTiWVCr RHEA and W films; (b) the illustration of 60 keV  $\text{He}^+$  beam injection machine; (c) the masked sample with tin foil to obtain unirradiated and irradiated regions, as shown in the representative optical profile image.

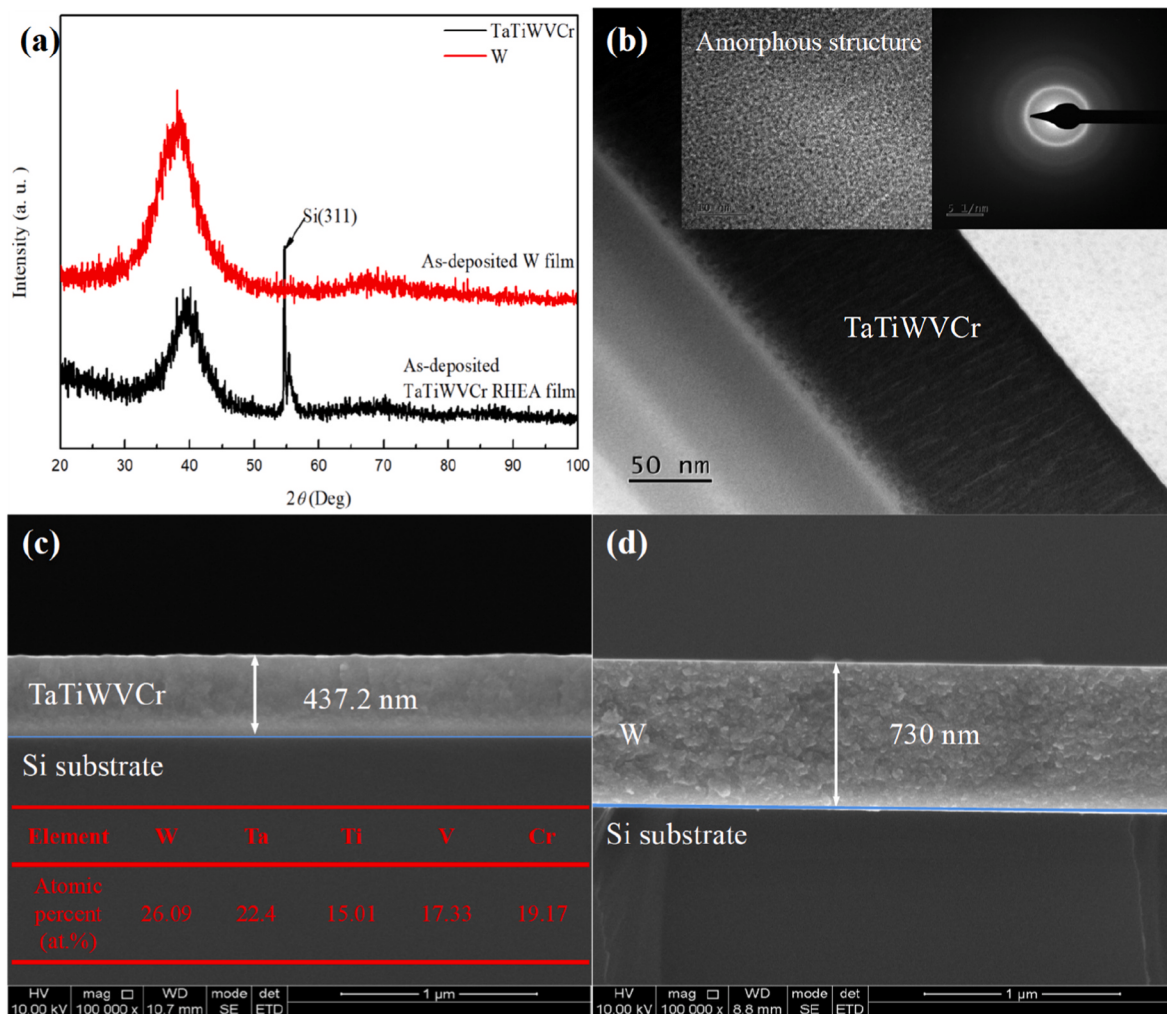


**Fig. 2.** (a) GIXRD spectra of as-deposited TaTiWVCr RHEA and W films; (b) the TEM images and inserted SAED image of TaTiWVCr RHEA; (c) the cross-sectional morphology of TaTiWVCr RHEA film; (d) cross-sectional morphology of W film.

composition elements (Ta, Ti, W, V and Cr) were included in this calculated target, and the threshold displacement energies ( $E$ ) were inquired in ASTM E521 (i.e.  $E_{\text{Ta}} = 90 \text{ eV}$ ,  $E_{\text{Ti}} = 30 \text{ eV}$ ,  $E_{\text{W}} = 90 \text{ eV}$ ,  $E_{\text{V}} = 40 \text{ eV}$  and  $E_{\text{Cr}} = 40 \text{ eV}$ ) [34]. Distribution profiles of irradiation damage and He atom concentration (in at. %) as function of implanted depth were calculated by the familiar equations [35]. Grazing Incidence X-ray Diffraction (GIXRD, Bruker D8 Advanced) with a Cu  $K\alpha$  radiation wavelength of 0.15418 nm was performed to characterize the phase structure in the RHEA and W films before and after irradiation, the GIXRD data were recorded at a grazing incidence angle of  $2^\circ$  for the angle scanning range of  $20^\circ$ – $100^\circ$  with a step of  $0.04^\circ$  and a dwell time of 0.3 s for each step. The micro-graph of surface topography, cross-sectional morphology and elemental composition of the as-deposited films were measured by the Scanning Electron Microscope (SEM, FEI Inspect F50) and Energy Dispersive X-ray spectroscopy (EDS, OCTANE SUPER), respectively. The profiles of interior structure and irradiation-induced defects were detected by High Resolution Transmission Electron Microscopy (HRTEM, Talos F200 $\times$ ; FEI Tecnai G2 F20). The Selected Area Electron Diffraction (SAED) was performed to characterize the phase-constructions of RHEA and W films after He $^+$  irradiation. Meanwhile, EDS (Super-X; Bruker Xflash 5030) was carried out to analyze the composition changes of irradiated samples. The TEM foils used for measurements were prepared by mechanical polishing, followed by ion milling to form a wedge to create sufficient electron transparency on a low-energy (0.5–2 keV) Ar ion polishing system. An Optical Profilometer (Super View W1,  $\times 10$  objective lens) was carried out to comprehensively characterize the evolution of surface modification and the irradiation-induced volume swelling of the irradiated films.

### 3. Results

#### 3.1. Micro-structure of as-deposited TaTiWVCr RHEA and W films

Fig. 2(a) shows the GIXRD spectra of as-deposited TaTiWVCr RHEA and W films. Broad diffraction peaks were observed in the two patterns, in which these broad peaks indicate the formation of amorphous structures in the TaTiWVCr RHEA and W film based on the full width at half maximum (FWHM,  $4.436^\circ$  and  $4.337^\circ$ , respectively). Fig. 2(b) shows the TEM images and the inserted SAED image. Disordered state can be observed from the inserted HRTEM image, and the inserted SAED image further certifies that the amorphous states are formed in the as-deposited TaTiWVCr RHEA film, which is well consistent with the GIXRD result. Average thickness of 437.2 nm in RHEA film was calculated from the cross-sectional morphology (Fig. 2(c)). The EDS results were detected from the cross-section by line scanning (the inserted Table), showing that the atomic percentages in compositions exhibit approximate equimolar ratio and a chemical homogeneity in the as-deposited RHEA film (Supplementary Fig. S1). Similarly, the amorphous structures can be also observed from the cross-section of as-deposited W film (Fig. 2(d)), which is well consistent with the GIXRD result.

The formation of crystalline structure in RHEA with complex composition is closely associated with the radius of solute atoms and the thermodynamic parameters. The atomic radius mismatch ( $\delta$ ) would prominently affect the solid-solution ability of each atom in multi-component alloy. On the one hand, the serious lattice distortion and the strain energy in the alloy matrix simultaneously increases due to the large  $\delta$ . Hence, the large  $\delta$  results in the enhancement of free energy in alloy, which would reduce the stability of solid-solution. On the other hand, the significant discrepancy in atomic size ratios causes sluggish diffusion of atoms in matrix, which reduces the phase transformation rate and makes the atoms segregate in alloy, even causes the formations of nanocrystalline and amorphous structures [12,36]. The mixing enthalpy ( $\Delta H_{\text{mix}}$ ) is the predominant part of the free energy, which determines the priority of intermetallic compounds or solid-solution phases formation. At the same time, the mixing entropy ( $\Delta S_{\text{mix}}$ )

contribution for solid-solution formation also has to be taken into account due to the high  $\Delta S_{\text{mix}}$  for multi-component alloys, the high  $\Delta S_{\text{mix}}$  can make random solid-solution form easily and more stable than intermetallic compounds or other ordered phases during solidification in alloys [12,36].  $\Omega$  is the Yang-Zhang parameter used to evaluate the balance between  $\Delta H_{\text{mix}}$  and  $\Delta S_{\text{mix}}$ . Four crucial parameters for the prediction of the solid-solution phase or the amorphous structure are shown by the following equations [12,36]:

$$\delta = 100 \sqrt{\sum_{i=1}^n c_i \left(1 - \frac{r_i}{\bar{r}}\right)^2} \quad (1)$$

$$\Delta H_{\text{mix}} = 4 \sum_{i=1, i \neq j}^n \Delta H_{\text{mix}}^{ij} c_i r_i \quad (2)$$

$$\Delta S_{\text{mix}} = -R \sum_{i=1}^n c_i \ln c_i \quad (3)$$

$$\Omega = \frac{T_m \Delta S_{\text{mix}}}{|\Delta H_{\text{mix}}|} \quad (4)$$

where  $n$  is the element numbers,  $T_m$  ( $T_m = \sum_{i=1}^n c_i T_{m,i}$ ) is the melting temperature,  $\Delta H_{\text{mix}}^{ij}$  is the mixing enthalpy of binary  $ij$  atomic pairs,  $c_i$ ,  $T_{m,i}$  and  $r_i$  are the atomic fraction, melting temperature and radius of the  $i$ th element, respectively,  $R$  is the gas constant (8.314 J/(mol·K)) and  $\bar{r}$  is the average atomic radius. The calculated  $\delta$ ,  $\Delta H_{\text{mix}}$ ,  $\Delta S_{\text{mi}}$ , and  $\Omega$  values are tabulated in Table 1. These calculated parameters of the TaTiWVCr RHEA can well meet the criteria of solid-solution phase formation [36]:  $-22 \leq \Delta H_{\text{mix}} \leq 7 \text{ kJ/mol}$ ,  $0 \leq \Delta S_{\text{mix}} \leq 8.5 \text{ J/(K·mol)}$ ,  $\delta \leq 6.6$  and  $\Omega \geq 1.1$ . Therefore, the deposited TaTiWVCr RHEA films tend to form stable solid-solution rather than amorphous structure according to these parameters. In this case, the as-deposited TaTiWVCr RHEA and W films exhibit amorphous structures, which can be explained by the non-equilibrium state and cooling rate during magnetron sputtering. At room temperature, those sputtered atoms do not acquire enough kinetic energy by collision for arriving ordered phase [37]. Also, the rapid cooling rate cannot provide sufficient time and energy for metal elements to fully redistribute and crystallize, the amorphous mixtures were tuned by appropriately adjusting the perpendicular distance  $L$  (Fig. 1(a)) and sputtering power during the deposition process.

#### 3.2. SRIM simulation of He ion irradiation response in TaTiWVCr RHEA and W

SRIM simulation is frequently utilized to calculate electronic and nuclear stopping powers in target atoms and to determine the inelastic and elastic energy transfer from an energetic incident ion to target atoms as the energetic incident ion transverses the target until it comes to a stable state [33]. Those produced vacancies or displacements are utilized to evaluate the irradiation damage in dpa resulting from certain dose of incident ions. An energetic ion loses energy through inelastic energy transfer to electrons (excitation and ionization of target atoms and the ion itself), elastic energy transfer to atomic nuclei (recoils), as well as high-energy effects (e.g., nuclear reactions and bremsstrahlung) [38]. The ratio of energy loss per unit path length ( $dE/dx$ ) is considered as stopping power, also known as stopping force of a target [38,39]:

$$\frac{dE}{dx} = NS(E) \quad (5)$$

**Table 1**

The thermodynamic parameters in TaTiWVCr RHEA film.

Thermodynamic parameters	$\delta$	$\Delta H_{\text{mix}}$ (kJ/mol)	$\Delta S_{\text{mix}}$ (J/(K·mol))	$\Omega$
TaTiWVCr RHEA	9.9	-5.06	13.58	7.13

$$S(E) = \int T d\sigma(E, T) \quad (6)$$

where  $N$  is the atom number in the target,  $S(E)$  is the stopping cross section,  $T$  is the total energy loss and  $d\sigma(E, T)$  is the differential cross section for energy loss at an ion beam energy ( $E$ ). In other words, ion energy loss is separated into (I) energy transfer to target electrons (electronic stopping power,  $dE/dx_e$ ) that causes ionization, and (II) energy transfer to target nuclei (nuclear stopping power,  $dE/dx_n$ ) that results in either atomic displacements or phonon energy dissipation [38]. Fig. 3(a and b) shows the  $dE/dx_e$  and  $dE/dx_n$  of He ion with the energy range of 0–10 MeV, which was simulated by the Stopping Rang (SR) programme in SRIM software. As shown in figures, the variations of  $dE/dx_e$  and  $dE/dx_n$  as a function of ion's incident energy display reverse tendencies, drastic evolution rules in these two parameters can be also observed when the incident energy is lower than 1 MeV, even the  $dE/dx_n$  is infinitely close to zero as the incident energy is higher than 1 MeV. The calculated  $dE/dx_e$  are 24.78 eV/Å and 28.64 eV/Å for 60 keV of  $\text{He}^+$  injected into TaTiWVCr and W targets, respectively. The values of  $dE/dx_e$  are considerably higher than the  $dE/dx_n$  (0.73 eV/Å for RHEA and 0.927 eV/Å for W). In a word, at the  $\text{He}^+$  energy of 60 keV, the  $dE/dx_e$  makes a main contribution to the energy dissipation of He ion during the collision cascade. The main energy dissipation in TaTiWVCr RHEA and W targets resulted from the electronic stopping powers is responsible for the formation of thermal-spike effect along the incident ions' trajectory [39]. Meanwhile, the electronic excitation and the

lattice damage were ascribed to a reduction of the thermal conductivity and an enhancement of the electron phonon coupling. Because of the nuclear collision-induced lattice defect, which suppresses dissipation of local excitation energy and further influences the electronic excitation created thermal spike effect and the irradiation damage level [38,39].

Fig. 3(c and d) shows average energy deposition as a function of implanted depth for 60 keV He ions in TaTiWVCr RHEA and W targets calculated by Transport of Ions in Matter (TRIM) program in SRIM software. Energy loss to the target electronic system ( $E_{\text{ionization}}$ ) is the sum of ionization losses by both ions and recoils. As reported [51], energetic recoils can further excite target electrons and induce cascade damage, the kinetic energy of incident ion will transfer to both target atoms and electrons, which are consequently divided into damage energy and ionization energy, respectively. Accordingly,  $E_{\text{ionization}}$  is referred as the total electronic energy transfer to target electrons from both ions and energetic recoils. The damage energy ( $E_{\text{Damage}}$ ) is the energy consumed to produce atomic displacements of target [40].  $E_{\text{Phonon}}$  is regarded as phonon energy dissipation. Therefore, the total energy deposition ( $E_{\text{Total}}$ ) is defined as  $E_{\text{ionization}} + E_{\text{Damage}} + E_{\text{Phonon}}$ . We note that  $E_{\text{ionization}}$  is mainly expected for the energy loss under 60 keV  $\text{He}^+$  irradiation, it is consistent with the calculated electronic stopping power  $dE/dx_e$ . The values of  $E_{\text{Damage}} + E_{\text{Phonon}}$  are related to the physical phenomena: atomic displacements and the energy dissipation through phonon vibration [40].

In the SRIM code, ion-triggered damage profiles are generally determined using two different approaches provided by available TRIM

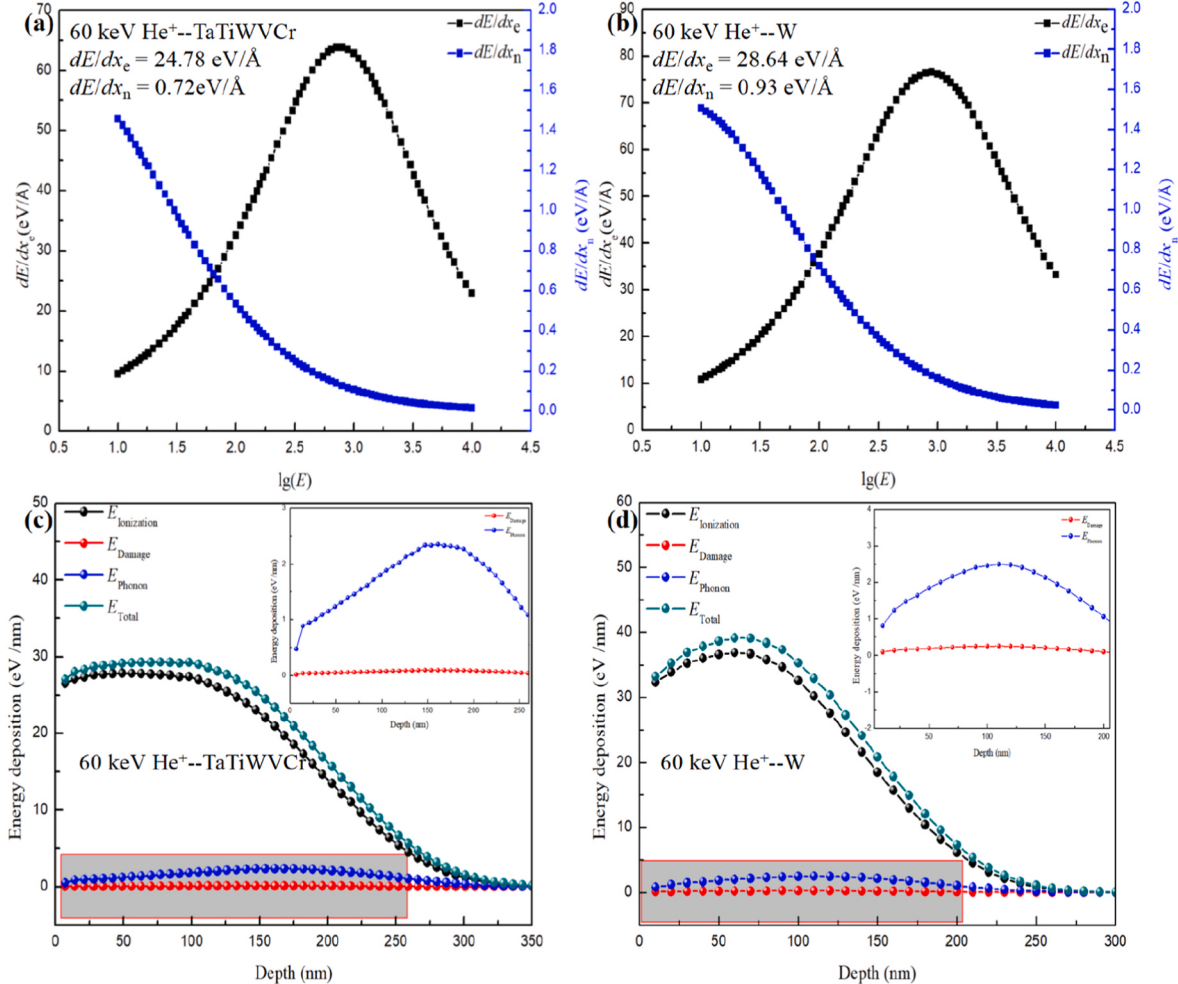


**Fig. 3.** (a–b) The electronic stopping power ( $dE/dx_e$ ) and nuclear stopping power ( $dE/dx_n$ ) of He ion incident into the TaTiWVCr RHEA and W within the energy range ( $E$ ) of 0–10 MeV; (c–d) the energy deposition per unit of depth for 60 keV He ions in the TaTiWVCr RHEA and W calculated by SRIM software.

options: (1) full-cascade TRIM calculation (Detailed Calculation with Full Damage Cascades), or (2) a quick TRIM calculation (Ion Distribution and Quick Calculation of Damage). For Full-cascade TRIM calculation, each recoil nucleus can be tracked until its energy is below the displacement threshold of the target atom. Meanwhile, the quick TRIM is based on the Kinchin-Pease mode regardless of the target damage details or sputtering. Weber et al. [33] considered that the full-cascade TRIM simulations provide a more accurate determination of damage energy, displacement numbers and damage depth profiles than the quick TRIM, especially for the multi-component targets. For a direct comparison of irradiation damage in the TaTiWVCr RHEA and W targets, the profiles of irradiation damage (dpa) and He concentration (at. %) are illustrated in Fig. 4 which calculated by the quick TRIM. As observed from Fig. 4(a), the irradiation damage in TaTiWVCr RHEA increase at first and then decrease with increasing of the implantation depth, a maximum value of 4.7 dpa located at depth  $\sim$ 160 nm is observed when the He<sup>+</sup> fluence is  $2 \times 10^{17} \text{ cm}^{-2}$ . Moreover, at the highest fluence of  $2 \times 10^{17} \text{ cm}^{-2}$ , we can find that the maximum He concentration (Fig. 4(b)) is approximately 16.5 at.% at the depth of 217 nm from Gaussian-like distribution curve of the implanted He concentration. By contrast, a maximum damage of 2.7 dpa (Fig. 4(c)) located at depth  $\sim$ 102 nm and He peak concentration of 18.4 at.% (Fig. 4(d)) located at depth of 150 nm are observed when the W exposed to the He<sup>+</sup> fluence of  $2 \times 10^{17} \text{ cm}^{-2}$ . These theoretical simulations indicate that the W exhibits a better irradiation resistance compared with the TaTiWVCr RHEA due to the low threshold displacement energies for Ti, V, Cr atoms and low stopping power [34].

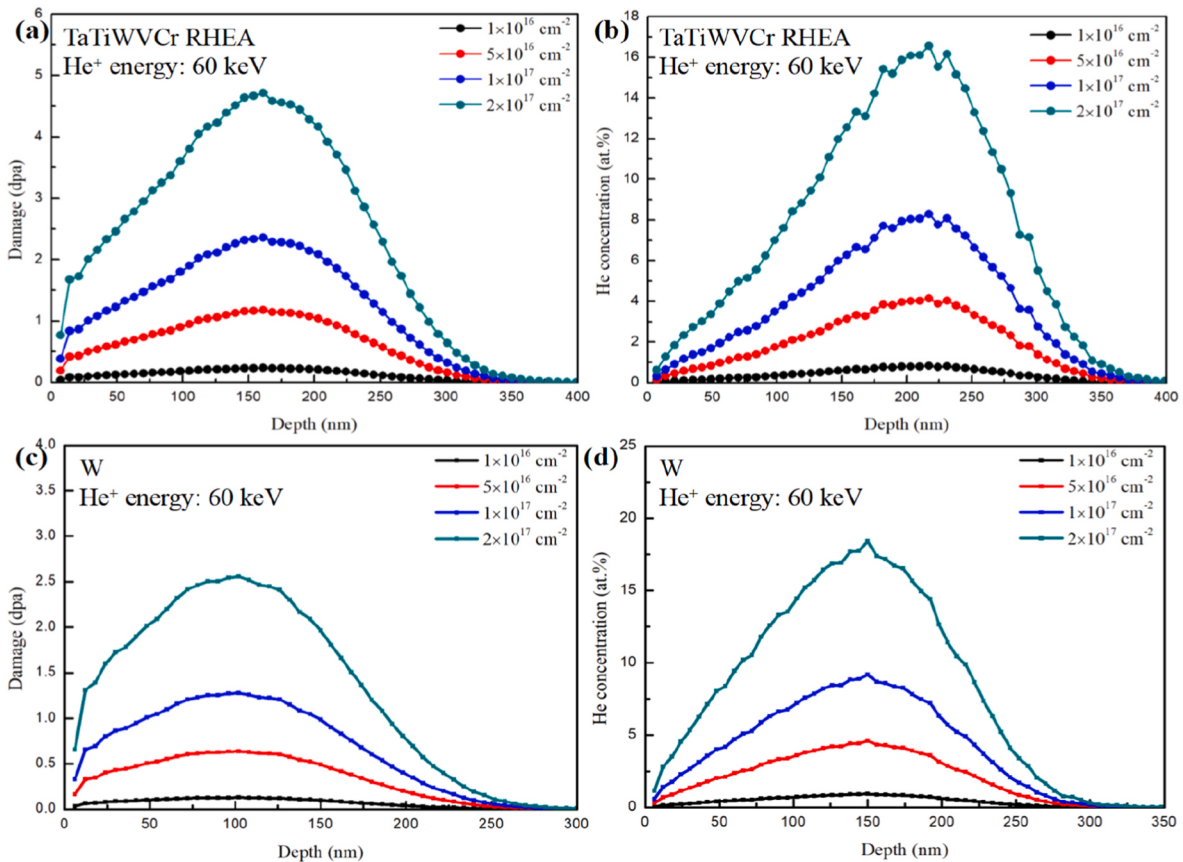


**Fig. 4.** (a) and (c) Depth profile of irradiation damage in the TaTiWVCr RHEA and W film irradiated by 60 keV He<sup>+</sup> at fluence ranging from  $1 \times 10^{16} \text{ cm}^{-2}$  to  $2 \times 10^{17} \text{ cm}^{-2}$  calculated by quick TRIM mode (SRIM-2013 software); (b) and (d) the corresponding implanted He concentration distribution in the TaTiWVCr RHEA and W film.

### 3.3. Micro-structure evolution and He behavior in irradiated TaTiWVCr RHEA and W films

Fig. 5 shows the GIXRD patterns of TaTiWVCr RHEA and W films after He<sup>+</sup> irradiation at fluence ranging from  $1 \times 10^{16} \text{ cm}^{-2}$  to  $2 \times 10^{17} \text{ cm}^{-2}$ . The broad peaks are still observed at fluence of  $1 \times 10^{16} \text{ cm}^{-2}$ , suggesting that the RHEA film remains amorphous state. At fluence of  $5 \times 10^{16} \text{ cm}^{-2}$ , sharp diffraction peaks appeared and overlapped with the broad peaks. This illustrates that the amorphous structure in RHEA transformed into nano-crystalline structure after He<sup>+</sup> irradiation. As the fluence further increased to  $1 \times 10^{17} \text{ cm}^{-2}$ , the peak intensities significantly increase, exhibiting a preferred growth orientation of BCC (110) crystallographic plane at this condition. Subsequently, the diffraction peaks present slight decrease at fluence of  $2 \times 10^{17} \text{ cm}^{-2}$  compared to the sample irradiated at  $1 \times 10^{17} \text{ cm}^{-2}$ . The decrease of peak intensity may attribute to the defect accumulation as the continuous enhancement of ion dose. Moreover, the broad peaks basically keep stable for the W samples irradiated at fluence ranging from  $1 \times 10^{16} \text{ cm}^{-2}$  to  $1 \times 10^{17} \text{ cm}^{-2}$ . While the obvious crystallization in W films was induced at the highest fluence of  $2 \times 10^{17} \text{ cm}^{-2}$ . It is worth to note that the growth of  $\gamma$ -W with face-centered cubic (FCC) structure was more preferentially induced than that of  $\alpha$ -W (BCC phase) after He<sup>+</sup> irradiation, the detailed phase structures will be further certificated by the following characterizations. The aforementioned results prove that the crystallization and grain growth in TaTiWVCr RHEA films are more easily occurred than the amorphous W films when exposed to the same He<sup>+</sup> environment.

The FWHM and the position of diffraction peak were analyzed according to the GIXRD patterns, as shown in Fig. 6. In comparison with the as-deposited film, the FWHM decreases with increasing fluences

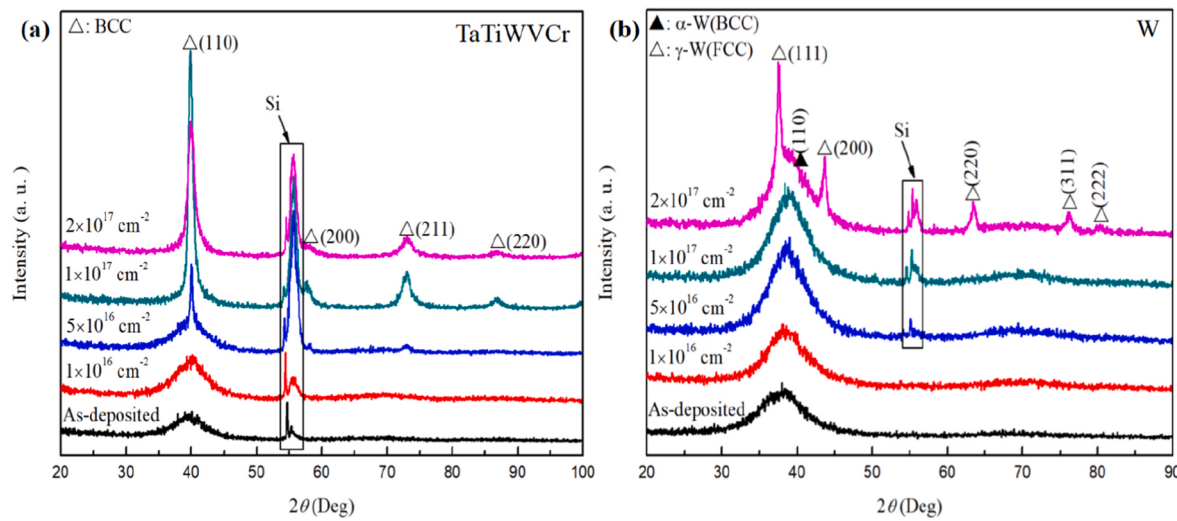


Fig. 5. GIXRD patterns of the TaTiWVCr RHEA and W films before and after He<sup>+</sup> irradiation.

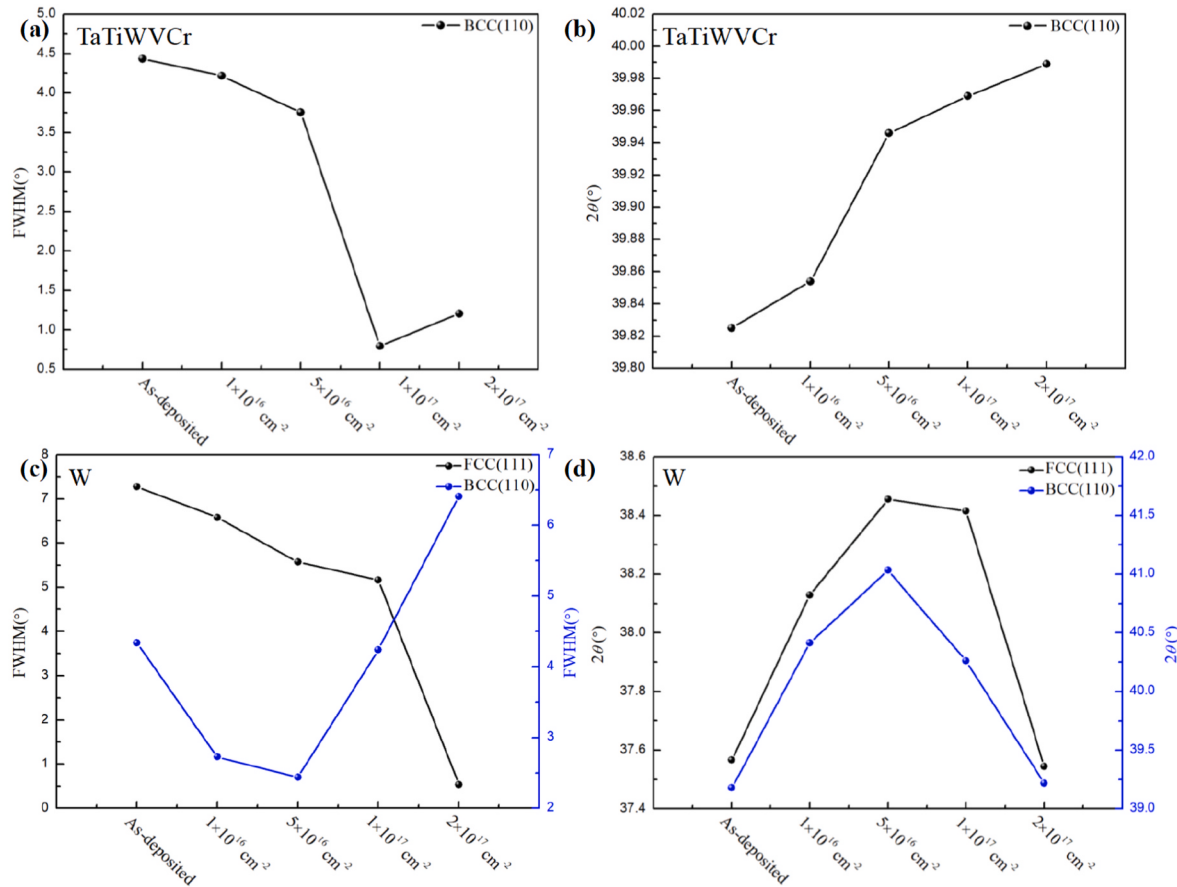


Fig. 6. (a) and (c) The full width at half maximum of TaTiWVCr RHEA and W films as a function of He<sup>+</sup> fluence; (b) and (d) the position variation of 2θ as a function of He<sup>+</sup> fluence.

from  $1 \times 10^{16} \text{ cm}^{-2}$  to  $1 \times 10^{17} \text{ cm}^{-2}$  (Fig. 6(a)). The grain size of 10.5 nm is calculated by Scherrer formula based on the FWHM ( $0.795^\circ$ ) of sample irradiated at fluence of  $1 \times 10^{17} \text{ cm}^{-2}$ . These significant growths of grain sizes indicate the irradiation-induced crystallization behavior under the combination effect including energy transfer of incident ion and solute migration [28–30]. However, a similar crystallization in AlNbTiZr medium-entropy alloy amorphous coating occurred which irradiated by 6 MeV Au-ions at higher fluence [41]. This crystallization

phenomena induced by heavy ion bombardment is ascribed to the irradiation-introduced thermal effect and local melting. In this case of 60 keV He<sup>+</sup> irradiation, the prominent electron stopping power and electron excitation induced ionization energy losses played vital role in producing inelastic thermal-spikes via electron-phonon coupling, prompting the local atoms' short range migration and rearrangements, as well as the consequent grain growth in TaTiWVCr RHEA films. The grain size of 6.9 nm (FWHM =  $1.207^\circ$ ) was formed at fluence of  $2 \times 10^{17}$

$\text{cm}^{-2}$  due to the defect accumulation inside the grains. The detailed defect characteristics will be presented in the TEM images. As the observation from Fig. 6(b), BCC (110) peak of RHEA continuously shifts to higher diffraction angles, indicating that the interplanar spacing was decreased by  $\text{He}^+$  irradiation. In contrast, for the irradiated W films, the FWHM of FCC (111) demonstrates reduction tendency with increasing fluences from  $1 \times 10^{16} \text{ cm}^{-2}$  to  $2 \times 10^{17} \text{ cm}^{-2}$  (Fig. 6(c)), and maximum grain size of 15.6 nm was calculated based on the FWHM ( $0.534^\circ$ ) of FCC (111). The FWHM of BCC (110) decreases at first and then increases, this may be due to the damage accumulated in BCC phase. Meanwhile, the diffraction peaks shift to high angle direction at fluence of  $1 \times 10^{16} \text{ cm}^{-2}$  and  $5 \times 10^{16} \text{ cm}^{-2}$ , and then shift to low angle direction as further increase fluences (Fig. 6(d)), indicating that the lattice spacing increased at first and then decreased. The lattice variations in the irradiated W films were most likely caused by the defects in elemental interstitials, such as He and W (self-interstitials).

Fig. 7 shows the interior micro-structure of TaTiWVCr RHEA films irradiated at fluence of  $5 \times 10^{16} \text{ cm}^{-2}$ . As shown in Fig. 7(a), the gray region represents the irradiated region, which is well consistent with the simulation depth (as shown in the inserted damage distribution curve). The SAED pattern with faint diffraction rings confirmed the coexistence of nano-crystalline and amorphous mixtures at this fluence, indicating that the crystallization phenomena and the grain growth in RHEA

initially occurred at fluence of  $5 \times 10^{16} \text{ cm}^{-2}$ . Fig. 7(c–e) shows the corresponding HRTEM images obtained from the damage peak region of TaTiWVCr films irradiated at fluence of  $5 \times 10^{16} \text{ cm}^{-2}$ , the randomly distributed nano-grains (marked by white dotted line) with sizes of 3–5 nm can be observed in matrix (Fig. 7(c)). Besides, the corresponding  $d$ -spacing ( $d_{\{110\}} = 2.2917 \text{ \AA}$ ) (Fig. 7(d)) and fast Fourier transform (FFT) images are also illustrated to certificate the crystalline structures. However, no He bubbles inside nano-grains are observed, because the high-density GBs can effectively annihilate point defects and disperse He atoms, leading to an inferior ability of bubble formation at this fluence. Moreover, the boundaries between nano-grains and amorphous zones are clear within the irradiated regions, meaning that the grain growth was promoted by the local atom rearrangement and the GB migration [30].

Fig. 8 shows the interior micro-structure of TaTiWVCr RHEA films irradiated at fluence of  $2 \times 10^{17} \text{ cm}^{-2}$ . As shown in Fig. 8(a), the enhanced crystallization and the grain growth were induced in the irradiated region, which was also certificated by the poly-crystalline diffraction rings in SAED image (Fig. 8(b)). From the enlarged TEM image in Fig. 8(c), abundant He bubbles (marked by red circles) are observed at the damage peak region of TaTiWVCr films which irradiated at fluence of  $2 \times 10^{17} \text{ cm}^{-2}$ . Moreover, partial stacking faults (marked by white rectangle) were also formed in the matrix. The representative

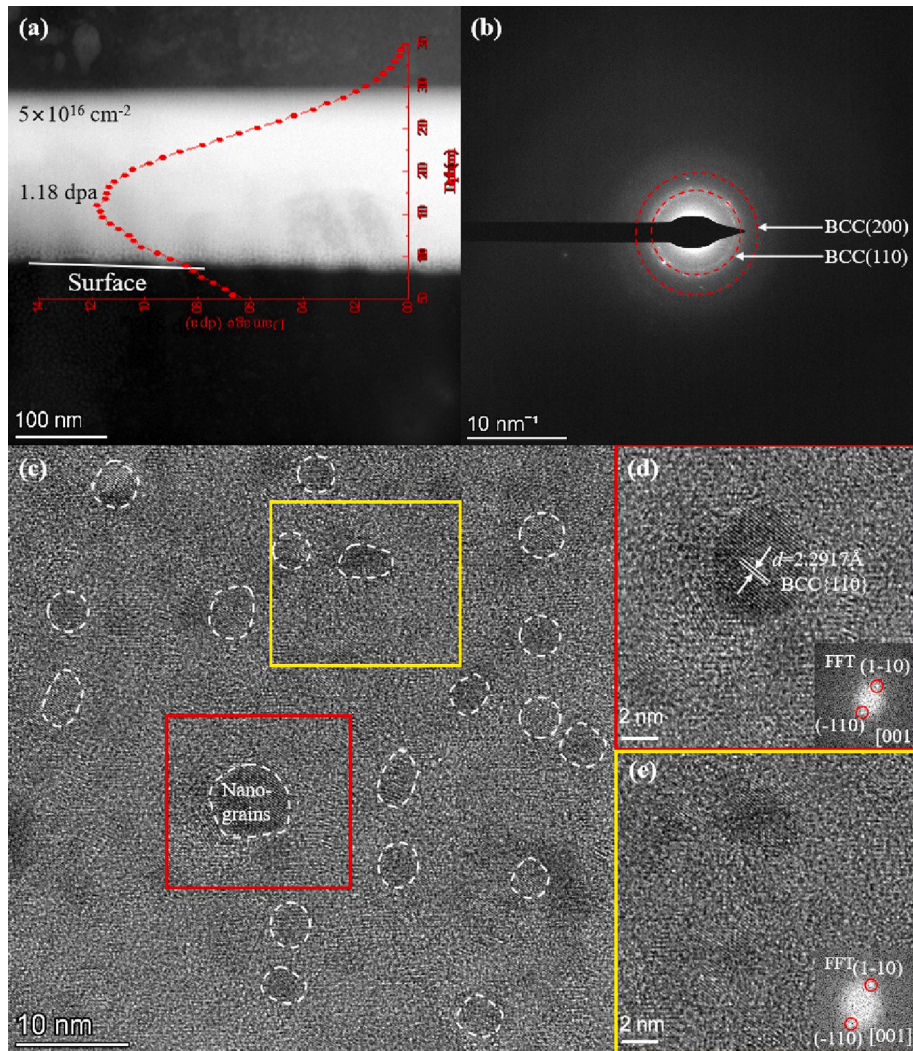


**Fig. 7.** Interior micro-structure of the TaTiWVCr RHEA irradiated at fluence of  $5 \times 10^{16} \text{ cm}^{-2}$ . (a) TEM image and inserted damage distribution curve; (b) SAED image obtained from irradiated region; (c) HRTEM images obtained from peak region, these white dotted lines represents nano-grains; and (d–e) HRTEM images obtained from the red and yellow rectangle regions in figure (c).

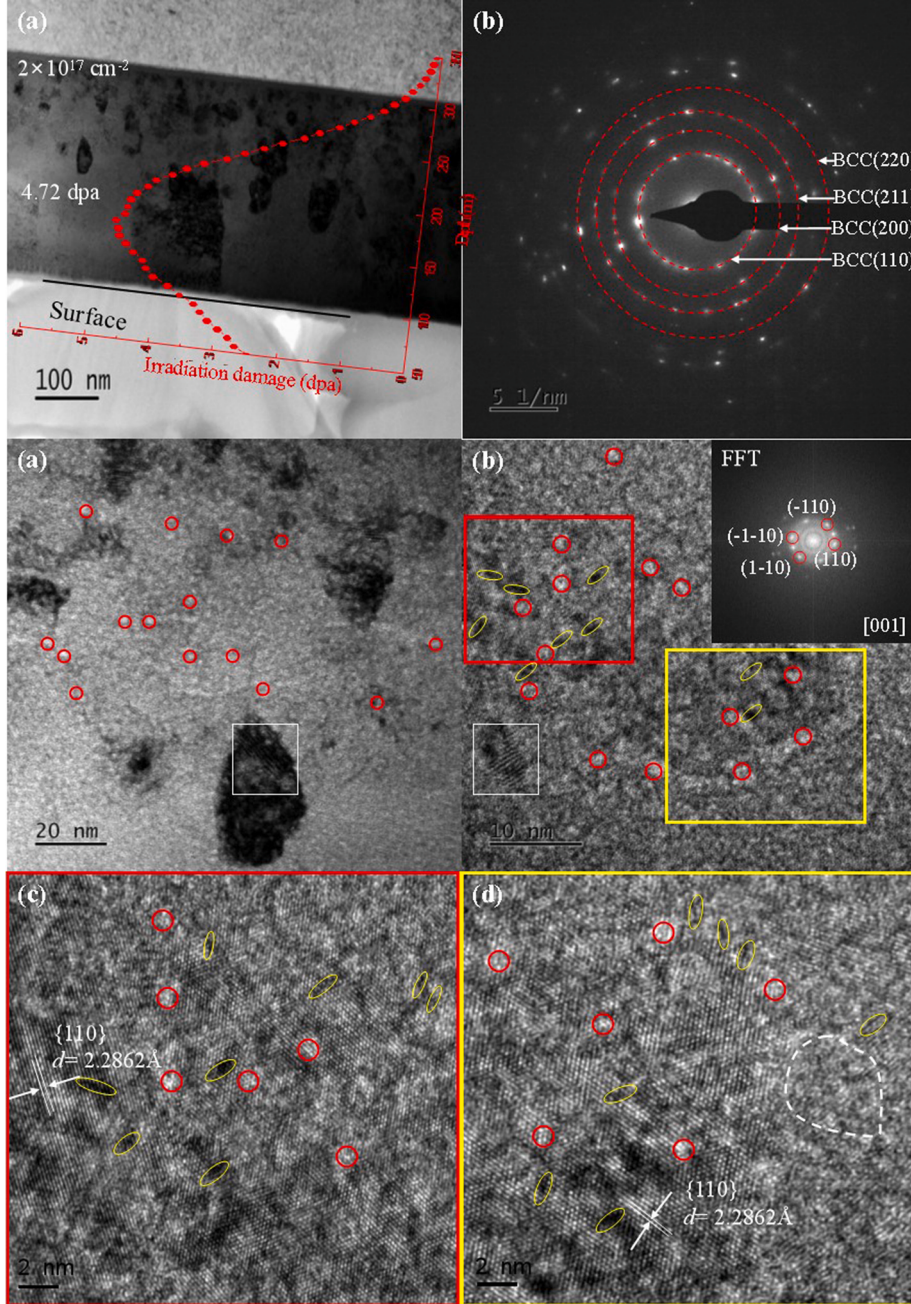


**Fig. 8.** Interior micro-structure of the TaTiWCr RHEA film irradiated at fluence of  $2 \times 10^{17} \text{ cm}^{-2}$ . (a) TEM image and inserted damage distribution curve; (b) SAED image obtained from irradiated region; (c) Enlarged TEM image; (d) HRTEM image and inserted FFT image obtained from peak region and (e–f) HRTEM images obtained from the red and yellow rectangles in (d). In the images, red circles represent He bubbles, yellow ellipses represent dislocations, the region of white solid line rectangle is stacking faults, the region of white dotted line rectangle is disordered structure.

HRTEM images of the irradiated TaTiWCr RHEA is shown in Fig. 8(d), those columnar grains were induced along the {110} direction. The average grain-size was increased to approximate 8.0 nm in comparison with that of RHEA film irradiated at fluence of  $5 \times 10^{16} \text{ cm}^{-2}$ , these results are basically consistent with the GIXRD characterization result (Fig. 5(a)). Based on the inserted FFT image, the BCC phase remain stable at this condition. To further certificate the crystalline structures, the corresponding lattice spacing of {110} is also displayed in the HRTEM images of Fig. 8(e and f), which obtained from Fig. 8(d) (marked by red and yellow rectangles). At the same time, small-sized dislocations (marked by yellow ellipses) can be observed, these dislocations may result from the combinations of vacancy accumulations inside the distorted lattices. Near the damage peak region, these He bubble clusters are mainly formed in the grains and at GBs, and finally cause the formation of disordered region again (marked by white dotted line in Fig. 8(f)). This observation may be attributed to two possible mechanisms. On

the one hand, the formed He bubbles in TaTiWCr film could undergo a coarsening process through a migration and coalescence mechanism, in which the small-sized bubbles can migrate through the random rearrangement of bubble surfaces by the diffusion of matrix atoms [42]. In the He concentration peak region, the high density and small spacing of He bubbles could accelerate the agglomeration of small-sized bubbles by such short-range migration, and the bubble clusters are formed. On the other hand, the irradiation-enhanced compositional fluctuation results in the formation of local elemental segregation or even clustering with increasing ion fluence. The chemical inhomogeneity could consider as strong sinks to entrap small-sized bubbles, which provide preferential nucleation and growth of He bubbles [19,31,32]. These two mechanisms may play synergistic roles to elucidate the formations of He bubbles and disordered regions in the TaTiWCr RHEA film irradiated at the highest fluence.

For a comparison, the internal micro-structure of W film irradiated at

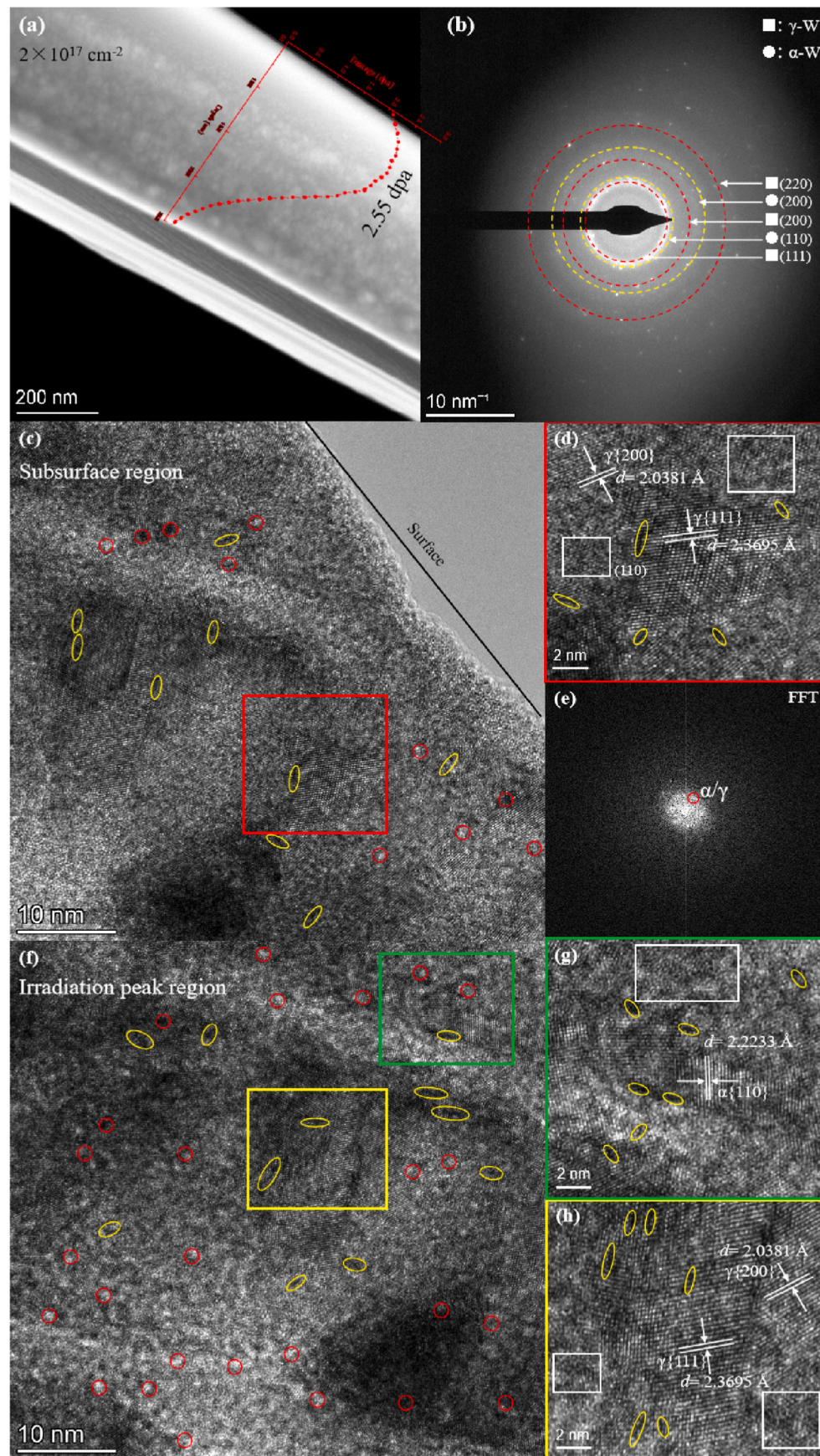


**Fig. 9.** Interior micro-structure of the W film irradiated at fluence of  $2 \times 10^{17} \text{ cm}^{-2}$ . (a) TEM image and inserted damage distribution curve; (b) SAED image obtained from irradiated region; (c) HRTEM image obtained from the subsurface region ( $\sim 100 \text{ nm}$  in depth); (d) HRTEM image obtained from the marked yellow rectangle region in (c); (e) FFT image obtained from (d); (f) HRTEM images obtained from the damage peak region ( $\sim 100 \text{ nm}$  in depth); (g-h) HRTEM images obtained from the marked green and yellow rectangles in (f). In the images, red circles represent He bubbles, yellow ellipses represent dislocations, the region of white solid line rectangle is disordered structure.

fluence of  $2 \times 10^{17} \text{ cm}^{-2}$  was also examined by TEM. As shown in Fig. 9(a), the nano-crystalline structures were detected from TEM. At the same time,  $\alpha$ -W and  $\gamma$ -W dual-phase structures were confirmed by polycrystalline diffraction rings in SAED image (Fig. 9(b)). At the subsurface region (Fig. 9(c)), the columnar grain was also induced and the grains with {111} direction exhibited preferential growth, and the average grain sizes was increased to 14.0 nm. Less bubbles (marked by red circles) and dislocations (marked by yellow circles) also distributed in the film matrix. The  $d$ -spacing ( $d_{\gamma\{111\}} = 2.3695 \text{ \AA}$ ,  $d_{\gamma\{200\}} = 2.0381 \text{ \AA}$ , see Fig. 9(d)) and FFT (Fig. 9(e) images are presented to identify the W phase structure. At the damage peak region (Fig. 9(f)), more large-sized bubbles and dislocations (marked by red circles and yellow ellipses) were induced due to the enhanced He concentration (The peak value is 18.4 at.%). Meanwhile, the lattice spacing of  $d_{\alpha\{110\}} = 2.2233 \text{ \AA}$  is also confirmed in Fig. 9(g), indicating that the coexistence of  $\alpha$ -W and  $\gamma$ -W grains was formed according to the above analysis. The disordered regions were induced by those agglomerated bubble clusters (marked by white dotted line in Fig. 9(d) and (g-h)). Noticeably, the bubble with larger size in W film was formed in comparison with the bubble morphology in TaTiWVCr RHEA film. When He ions implanted into the W film, stress was produced as a result of irradiation-induced defects, this stress increased with increasing fluence. Lattice distortion, amorphization or polycrystallization are various pathways to release stress [43]. Phase transformation is also treated as an effective approach to release interior stress through the migration of W atoms [44]. Subsequently, the growth of  $\gamma$ -W was more preferentially induced than that of  $\alpha$ -W under the certain irradiation conditions.

### 3.4. Comparison of bubble characteristic in irradiated RHEA and W films

Based on the aforementioned TEM observations, the bubble size distribution in irradiated regions were analyzed to further assess the He behavior characteristic. The statistical results of bubble size, bubble pressure and He number in bubbles are illustrated in Fig. 10. The average diameters of 2.6 nm in RHEA film and 3.3 nm in W film were measured by statistical software, as shown in Fig. 10(a) and (b). Obviously, both the morphology and the statistical results disclosed that the smaller-sized bubbles were formed in RHEA than that of metal W, indicating that the bubble sizes are prone to increase in the W film. Based on the bubble size distribution, several reasons have been put forward to interpret the superior tolerance to bubble formation introduced by the complex chemistry in RHEA. Firstly, the energy barriers of complicated defect in RHEA can modify the defect kinetics [31]. Specifically, interstitial mobility is substantially decreased while the vacancy mobility is increased, which shorten the migration gap between point defects and facilitate their inter-recombination; as a result, fewer vacancies are available for bubble growth [44]. Secondly, the complicated chemistry of RHEA produced lattice distortion helps to trap He atoms and suppress its long-range diffusion [45,46]. Thirdly, the chemical complexity in alloy can suppress the evolution and emission of dislocations around bubbles, leading to the smaller bubble sizes [32]. These explanations could cooperatively contribute to the lower growth rate for those bubbles in more chemically complicated RHEA compared to the bubble size in W films.

The existed researches [25,26] revealed that He bubbles with high internal pressure can evoke drastic strain field, which drastically affects the adjacent defects production and micro-structure evolution in the

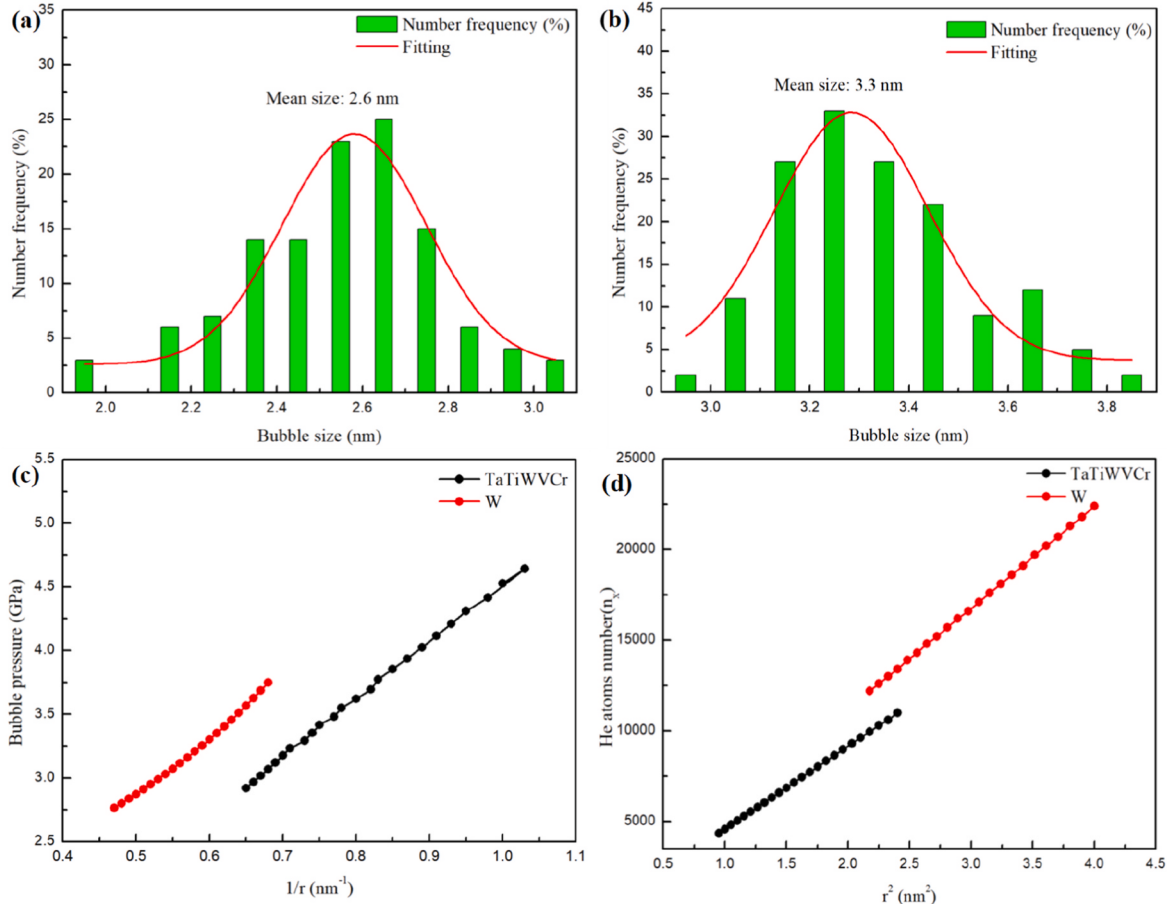


**Fig. 10.** (a–b) Size distribution of He bubbles in the TaTiWVCr RHEA and W films irradiated at fluence of  $2 \times 10^{17} \text{ cm}^{-2}$ ; (c) The pressure inside He bubbles in the TaTiWVCr RHEA and W films as a function of the inverse radius; (d) He atom numbers inside bubbles as a function of the radius squared.

irradiated materials. As for the He bubbles under equilibrium conditions, the bubble pressure is related to its size and the surface energy of matrix, the bubble pressure ( $P$ ) can be roughly calculated by the Young-Laplace equation [47]:

$$P = 2\gamma_{SV}/r \quad (7)$$

where  $\gamma$  is the surface free energy,  $r$  is the bubble radius. The pressures inside the bubbles are inversely proportional to the bubble radius. The surface energy  $\gamma_{SV}$  for the TaTiWVCr RHEA was calculated to be about  $2.2628 \text{ J m}^{-2}$ , which was acquired by averaging the surface energy of each individual-composition, the  $\gamma_{SV}$  of individual-composition [48] is displayed in Table 2. As illustrated in Fig. 10(c), the bubble pressures in RHEA film are 2.92–4.64 GPa, and the pressures in W film are 2.77–3.75 GPa. Especially, even though the bubble size in RHEA is lower than that of the W film, the enhanced pressure is demonstrated inside the RHEA film, in which the smaller bubble size contributes to the enhanced bubble pressure compared to the bubble pressures in W film. The smaller bubbles have extremely high pressures, an upper bound limit was determined by the materials properties to effectively describe the bubble pressures, which can be expressed by

$$P \leq 0.2\mu \quad (8)$$

where  $\mu$  is shear modulus ( $\mu_{RHEA} = 60.079 \text{ GPa}$ ,  $\mu_W = 145.42 \text{ GPa}$ ) [49]. The calculated upper limit of bubble pressure in RHEA and W are 12.0 GPa and 29.1 GPa, respectively, above which the He bubbles are mechanically unstable and the subsequent bubble growth will be dominated by dislocation punching [47]. There are two qualitatively explanations for smaller bubbles to coarsen into larger-sized bubbles. One mechanism is bubble migration and coalescence, and the other is Ostwald ripening, which is due to the thermally activated dissolution of small bubbles and the reabsorption of vacancies and He atoms to form large-sized bubbles again [50]. The sluggish diffusion of small-sized bubble can contribute to the increased bubble pressure in the RHEA compared with that of W films. Previous simulations showed that the high bubble pressure in complex chemistry alloy can reduce vacancies surface diffusion and consequently restrict their mobility [32]. In addition, simulation result found that the vacancy dissociation energy from a He-vacancy cluster can increase with increasing He density inside the bubble, so a high pressure can stabilize vacancies and inhibit the dissolution of small He bubbles [31]. These are important reasons to understand that why chemical complexity in RHEA films can increase the pressures inside the bubbles.

A bubble model was proposed to estimate the relationship between the number of He atoms in a bubble and its radius. An idea gas model was generally utilized to describe the bubble state [25,26,51]. Assume there  $n_x$  is atom number in a spherical bubble with a radius of  $r$  and the  $\rho_g$  is gas density. Then:

$$n_x = (4/3\pi r^3)\rho_g \quad (9)$$

$$PV = nkT \quad (10)$$

Using equation (2) $\gamma_{SV}/r$  for mechanical equilibrium to eliminate  $\rho_g$  and  $P$  in equations (9) and (10) gives:

$$n_x = 4 \left/ \frac{3\pi r^3}{rkT} \right. \frac{2\gamma}{r} = \frac{8\pi r^2 \gamma}{3kT} \quad (11)$$

where the  $k$  represents boltzmann constant ( $k = 1.3806 \times 10^{-23} \text{ J/K}$ ), and the  $T$  is irradiation temperature (about 300 K). As shown in Fig. 10

(d), the approximated number of He atoms  $n_x$  are in the range of  $\sim 4.35 \times 10^3$ – $1.10 \times 10^4$  inside bubbles based on the bubble diameter range in the irradiated TaTiWVCr RHEA film. Meanwhile, the  $n_x$  are in the range of  $\sim 1.22 \times 10^4$ – $2.24 \times 10^4$  inside bubbles for the irradiated W film calculated from the diverse bubble diameters.

### 3.5. The composition changes in irradiated TaTiWVCr RHEA films

The representative EDS mappings were detected from the TaTiWVCr RHEA films which irradiated at fluence of  $5 \times 10^{16} \text{ cm}^{-2}$ . As illustrated in Fig. 11(a–e), a homogeneous distribution in composition is observed in the mappings without dramatic composition enrichment and depletion. To clearly affirm the variation of, a line scanning result is shown in Fig. 11(f). A slight fluctuation ( $\pm 10$  at%) of element composition can be observed in the RHEA films. Radiation-induced segregation (RIS) generally occurred at large-sized defect sinks, such as large-sized bubbles, cavities and dislocation loops [52–54]. This possibility can be negated in this case since the undetectable bubbles in the irradiated region. The slight fluctuation of composition may attribute to the atom short-range migration to promote grain growth. At this condition, irradiation-enhanced nano-grains produced in RHEA film (see Fig. 7(c)). Those high-density GBs play crucial effect in decreasing the RIS level by inhibiting the point defects and facilitating the interstitial/vacancy recombination, leading to the suppression of solutes enrichment and depletion at the defect sink, which well agrees with the limited RIS in the ultra-fine Al<sub>1.5</sub>CoCrFeNi HEA after He<sup>+</sup> irradiation and in the nano-crystalline CoCrCuFeNi HEA after electron irradiation, respectively [22,55]. Fig. 12(a–e) displays the composition mappings of EDS measured from the TaTiWVCr RHEA films which irradiated at  $2 \times 10^{17} \text{ cm}^{-2}$ . From the mapping images, each of these elements present different levels of enrichment or depletion at the local region, as marked by the white circles. Simultaneously, according to the line scanning results in Fig. 12(f), the significant fluctuations ( $\pm 20$  at% -  $\pm 40$  at%) of element compositions were induced in the RHEA films, indicating that enrichment or depletion of elements occurred in a short range due to the sluggish diffusion. This inhomogeneous segregation can be explained by the over-pressurized He bubble-driven solute segregation in a short-range [26]. One similar report also disclosed that He atoms aggregated high-pressure bubble can enhance the heterogeneity of diffusivities and a low RIS level in the multi-component alloys [52]. The irradiation-enhanced crystallization could simultaneously result in the element rearrangement and the subsequent heterogeneity in composition.

### 3.6. Comparison of volume swelling of irradiated TaTiWVCr RHEA and W films

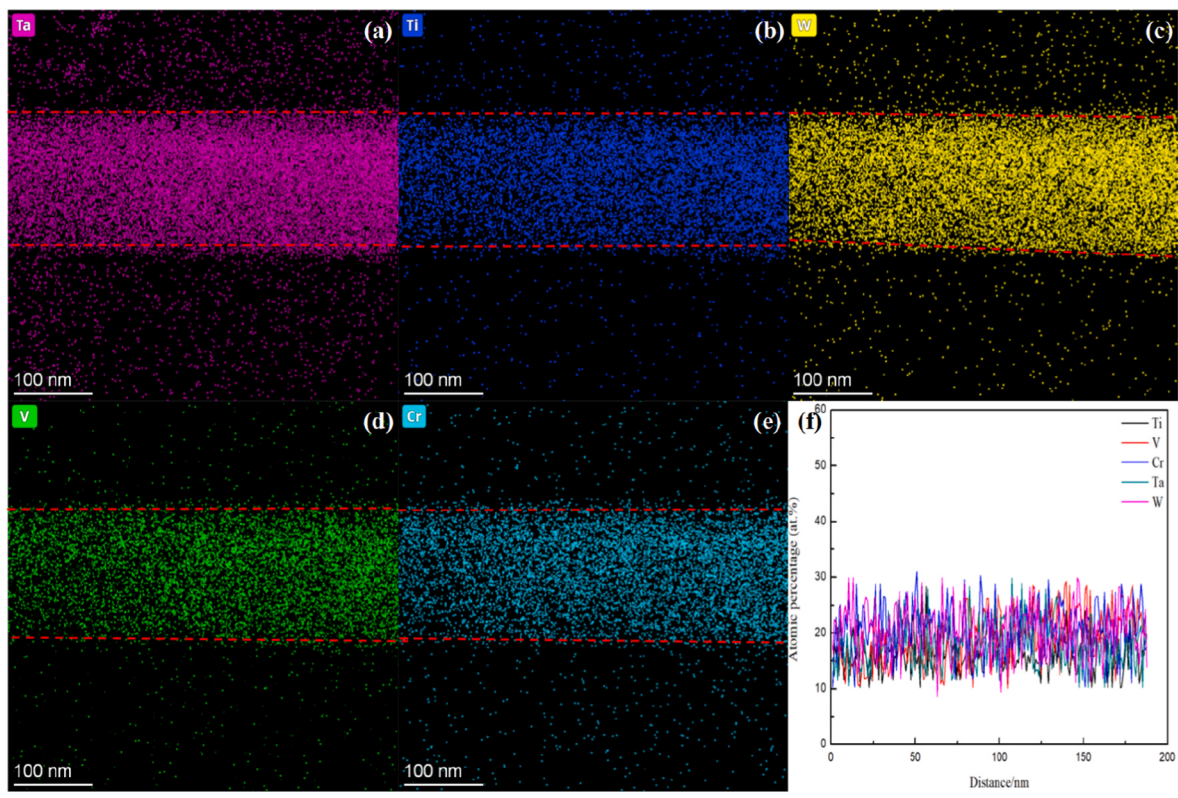
The three-dimensional (3D) morphology characteristics of the TaTiWVCr RHEA films after He<sup>+</sup> irradiation were obtained by the optical profiler, as shown in Fig. 13. From the 3D images (Fig. 13(a–d)), these obvious bulges represent surface blisters (marked by black arrows) while less blister bursts are formed (marked by white arrows) on the surface of irradiated regions. The color variations on the surface of irradiated regions indicate the bulge height of blisters and the superficial damage, and the conspicuous step-height plateaus between the irradiated region and the mask region can be observed in these irradiated RHEA films. The step-height plateaus can be regarded as the variation of volume swelling. Similarly, the 3D morphology characters of the irradiated W films were also obtained by the optical profiler, as shown in the Supplementary of Fig. S2, except for the surface blisters and blister bursts, an obvious mass migration (the red region near the step edge) happened on the irradiated region of W film due to the ion irradiation induced surface diffusion effect [44].

Fig. 14(a and b) presents height profiles for irradiated TaTiWVCr RHEA films and W films at different fluences, in which the step edges between the irradiated and masked regions (unirradiated) are sharp

Table 2

The surface energy  $\gamma_{SV}$  of all elements [48].

Element	Ta	Ti	W	V	Cr
Surface energy, ( $\gamma_{SV}$ J·m <sup>-2</sup> )	2.493	1.749	2.765	2.301	2.006



**Fig. 11.** (a–e) The EDS mapping of composition change in TaTiWVCr RHEA irradiated by 60 keV  $\text{He}^+$  at fluence of  $5 \times 10^{16} \text{ cm}^{-2}$ ; (f) the composition changes obtained by EDS line scanning.

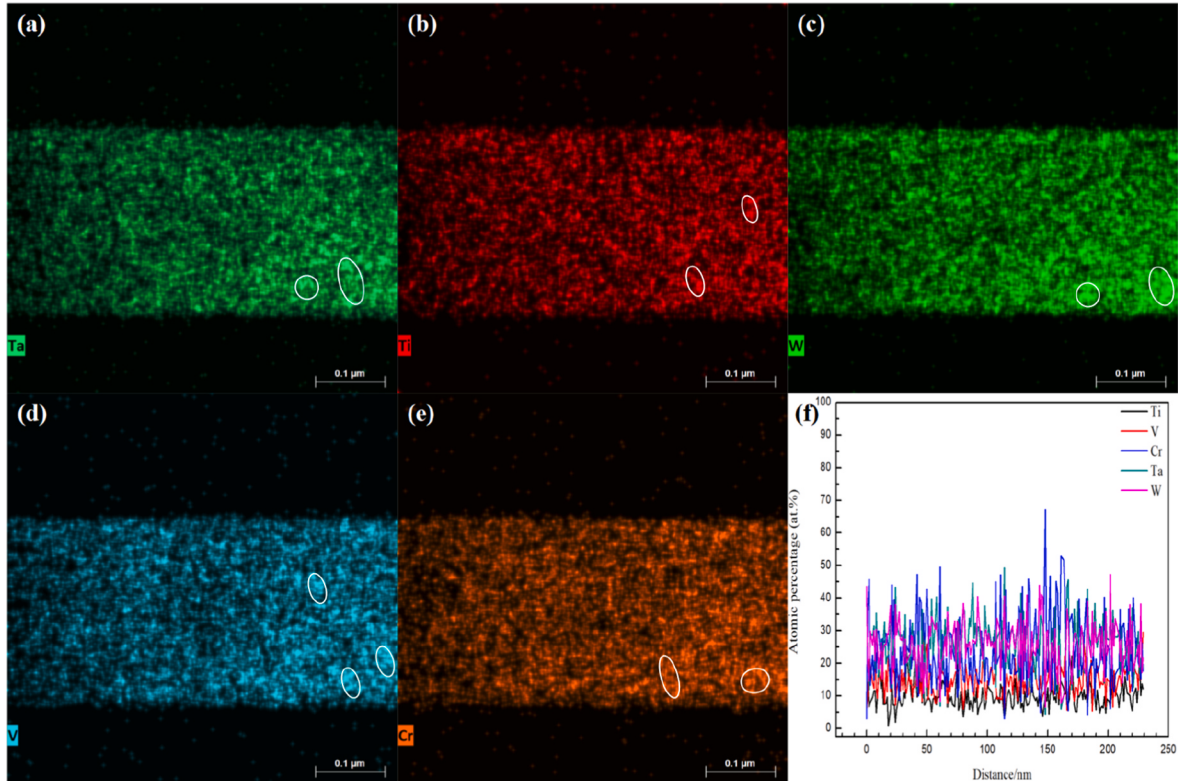


**Fig. 12.** (a–e) The EDS mapping of composition change in TaTiWVCr RHEA irradiated by 60 keV  $\text{He}^+$  at fluence of  $2 \times 10^{17} \text{ cm}^{-2}$ ; (f) the composition changes obtained by EDS line scanning.

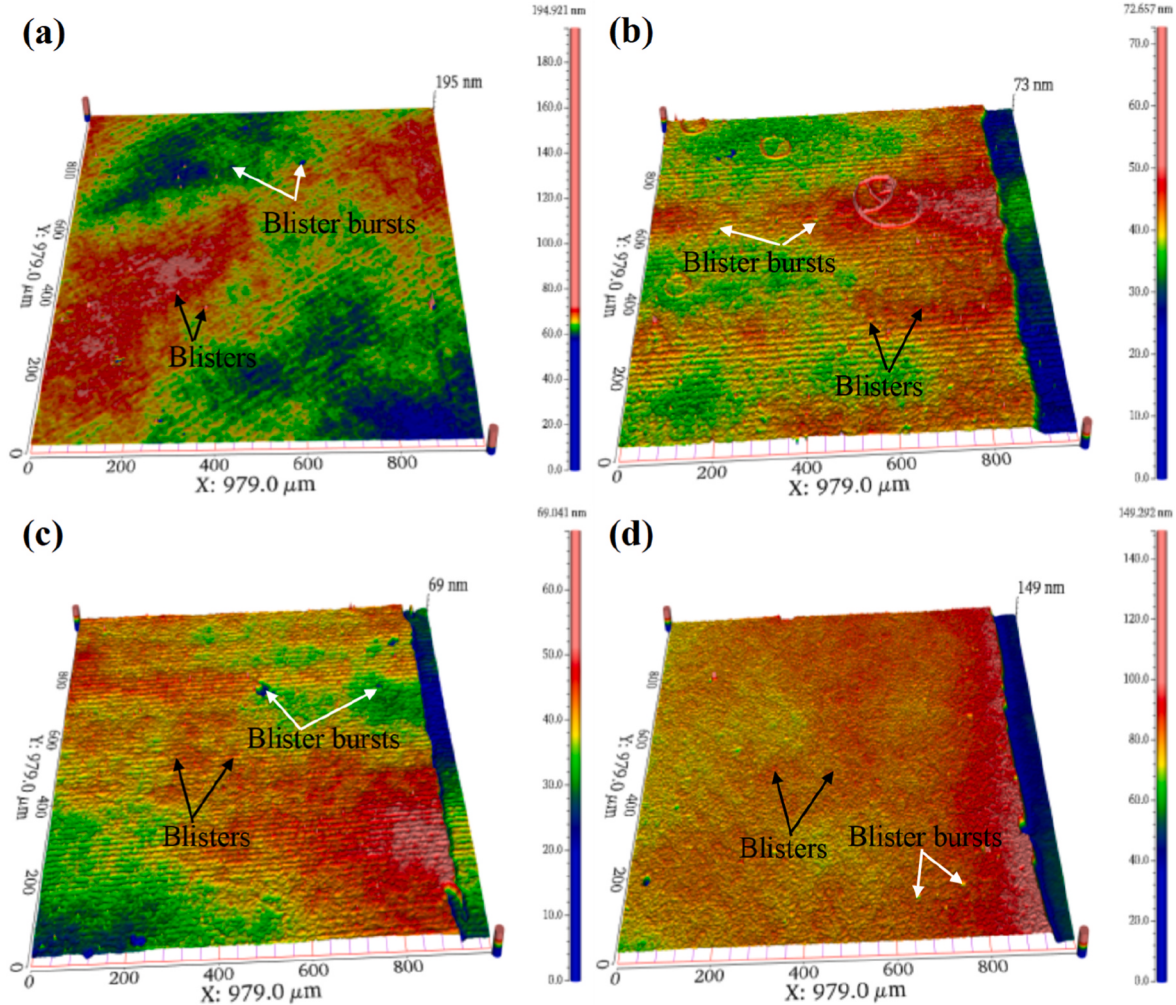


**Fig. 13.** Optical profile images of TaTiWVCr RHEA films irradiated at fluence of (a)  $1 \times 10^{16} \text{ cm}^{-2}$ , (b)  $5 \times 10^{16} \text{ cm}^{-2}$ , (c)  $1 \times 10^{17} \text{ cm}^{-2}$ , (d)  $2 \times 10^{17} \text{ cm}^{-2}$ .

with increasing fluence. The height profile differences  $\Delta H$  between the irradiated and unirradiated regions were calculated and illustrated in Fig. 14(c), revealing that the  $\Delta H$  has approximate values for these two kinds of materials irradiated at fluence ranging from  $1 \times 10^{16} \text{ cm}^{-2}$  to  $1 \times 10^{17} \text{ cm}^{-2}$  within the allowed error range. However, the  $\Delta H$  in W films is significantly higher than that of RHEA film which irradiated at fluence of  $2 \times 10^{17} \text{ cm}^{-2}$ . The measurements of step-height also provide an integrated swelling within the ion irradiated range. The volume swellings of these films irradiated to various fluences were calculated based on the ASTM standard E521-9615 using the following equation [56]:

$$S(\%) = \frac{\Delta H}{L} \quad (12)$$

where  $L$  is the implanted depth in the RHEA film (about 350 nm) and W film (about 300 nm). The calculated swelling includes lattice enhancement induced by He bubbles and surface blisters due to a shallow ion-implantation depth. As shown in Fig. 14(d), the swelling in the RHEA films increased from  $3.028 \pm 0.30\%$  to  $12.341 \pm 1.23\%$  at fluence ranging from  $1 \times 10^{16} \text{ cm}^{-2}$  to  $2 \times 10^{17} \text{ cm}^{-2}$ , while the swelling ( $3.436 \pm 0.34\%$ - $25.617 \pm 2.56\%$ ) in the W films are higher than that of RHEA films. These results indicate that the RHEA films display higher swelling resistance in comparison with the W films due to the small-sized bubbles and its dispersed distribution character in RHEA matrix. Except for the large-sized bubbles in W films, the surface blisters and the superficial atom migrations also effectively contribute to the increased swelling because of its lower implantation depth than that of RHEA

films.

#### 4. Discussion

##### 4.1. Bubble characteristics induced by the vacancy-dominated diffusion behavior

After energetic  $\text{He}^+$  irradiation by elevated fluences, introduction of He atom is accompanied by the displacement damage, namely, generating a mass of point defects (vacancy and interstitial) in metallic or alloy matrix [20–22,33]. Because of the finite solubility of He atoms in metallic or alloys, the implanted He will diffuse and combine with vacancies to form clusters or bubbles, in turn, the behaviors of point defect including its energy barrier and mobility will possess a dramatic impact on the He bubble distribution as well as its size characteristics [19,47]. According to the observation of TEM images, undetectable bubbles were formed at the fluence of  $5 \times 10^{16} \text{ cm}^{-2}$ . In this case, He atoms mainly occupied the interstitial sites in amorphous matrix and less vacancy was introduced in the nano-grains. Nevertheless, the He atoms are more easily combine with the irradiation-induced vacancies to form bubbles at the fluence of  $2 \times 10^{17} \text{ cm}^{-2}$ . In Table 3, the vacancy formation energy ( $E_V^f$  (eV)), vacancy migration energy ( $E_V^M$  (eV)) and vacancy activation energy of self-diffusion ( $E_{SD}^V$  (eV)) for the each elements were summarized according to the first-principles calculation [57]. McAlpine [58] simulated the vacancy formation energy distribution is ranging from 2 eV to 3.75 eV for the TaTiWVCr RHEA. Especially, the lowest

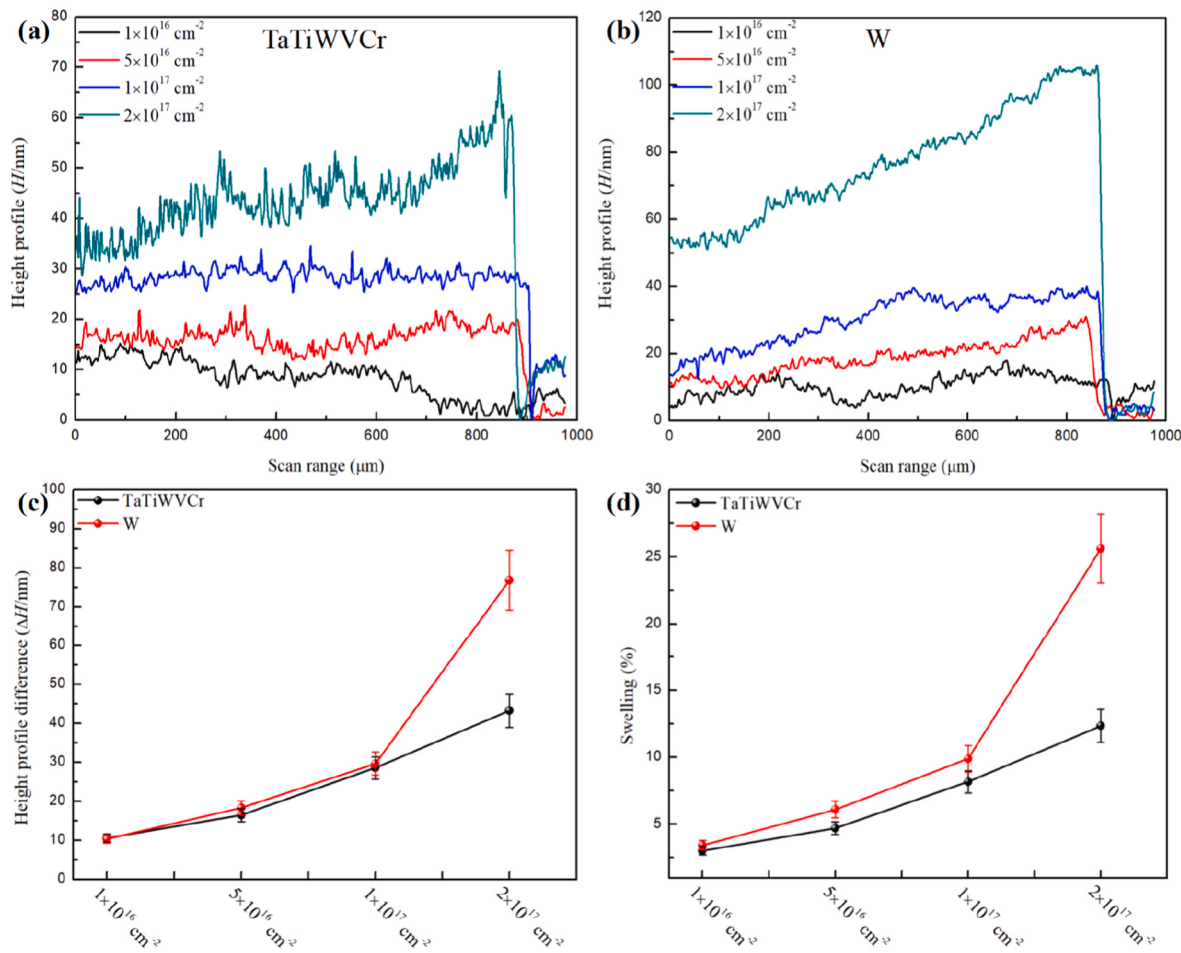


**Fig. 14.** (a–b) The height profile ( $H$ ) as a function of scanning range obtained from the irradiated TaTiWVCr RHEA and W films; (c) the height profile difference ( $\Delta H$ ) as function of He<sup>+</sup> fluence; (d) irradiation-induced swelling as function of He<sup>+</sup> fluence.

**Table 3**

The featured energy barriers for vacancy defects in the each element [57].

Element	Ta	Ti	W	V	Cr
Vacancy formation energies $E_V^F$ (eV)	3.12	2.07	3.27	2.66	2.93
Vacancy migration energies $E_V^M$ (eV)	0.75	0.47	1.82	0.46	0.90
Vacancy activation energy of self-diffusion $E^{SD}$ (eV)	4.14	2.48	5.54	3.30	4.08

energy at vacancy sites will be activated at low temperatures while the entire distribution of vacancies will be activated at high temperatures [59], causing diverse defect behavior at different irradiation scenarios. Previous simulation result [60] suggested that the energy barriers of the point defects exhibit a wide distribution because of lattice distortion and complex composition in multi-principal element alloys, and the overlap of migration energies for the interstitials and vacancies would facilitate the defects annihilation in multi-principal element alloys. This means that the mutual annihilation of point defects would be locally improved in the RHEA so that its vacancy concentration caused by the displacement damage will be lower than that of W. Furthermore, the vacancy concentration will increase to a supersaturation state with increasing the irradiation fluence, the featured energetics of point defects in the RHEA will intensify the annihilation of point defects or evolve into dislocations, stalking faults during He<sup>+</sup> irradiation.

In the practical situation, He diffusion would be very complicated and profoundly influenced by the irradiation conditions. H. Trinkaus [61] proposed that the He diffusion in metals or alloys mainly proceeds

by three modes of the interstitial migration, the vacancy migration, and the dissociation mechanism by the thermal activation and some collision displacement. In our situation where a considerable irradiation damage exposed to the He<sup>+</sup> fluence of  $2 \times 10^{17} \text{ cm}^{-2}$ , the irradiation-produced displacement and ionization-induced thermal-spike effect play synergistic role in increasing vacancy concentration. Hence, the irradiation enhanced vacancy contributes to the He diffusion and the combination of He-vacancy. Therefore, the effective He diffusivity  $D_{He}^{eff}$  could be expressed as [62]:

$$D_{He}^{eff} = C_V * D_V \quad (13)$$

where  $C_V$  is the vacancy concentration and  $D_V$  is the vacancy diffusivity. Considering the scenario of thermal equilibrium, in which the formula of (3) could be briefly described as:

$$D_{He}^{eff} = D_0 \exp(E_V^F + E_V^M) \quad (14)$$

where  $D_0$  is the pre-factor as generally stated. From above expression, the He diffusivity would depend on the energy barrier of vacancy in the RHEA. The aforementioned discussion demonstrates that the energy barriers for He-vacancy will enhance the recombination of point defects in RHEA, the higher vacancy formation energy could form a lower thermal vacancy concentration. Accordingly, the total vacancy concentrations in the irradiated RHEA are expected to be pretty lower than that of the irradiated W. Meanwhile, this discussion on He diffusion behavior can also obtain convincing confirmations from the bubble distribution and its size in TEM images (Figs. 8 and 9). It is well known

that implanted  $\text{He}^+$  usually exhibit a Gaussian-like distribution along the incident depth, and the He distribution will broaden at the elevated fluence due to the drastic diffusion effect. In current case, a wider distribution of He bubbles in the W film when comparing at the same irradiation condition, it indicates that the He atoms could rapidly transport far away from the damage peak region and contribute to the He bubble formation at the less damage region. Therefore, we deeply consider that the He diffusivity in the RHEA is expected to be lower than that of W.

To elucidate the bubble formation and establish the relationship between He diffusivity and the formation characteristics of He bubbles, the kinetic rate equations and classical nucleation theory were proposed to explain the bubble evolution [61,62]. According to the nucleation theory, a dual-atomic nucleation model will dominate the He bubble evolution at low temperature and/or high He production rate conditions, in which the He bubble number density ( $C_B$ ) and bubble size ( $r_B$  of the average bubble radius) will comply with the following asymptotic behavior [63]:

$$C_B \propto \left[ (D_{\text{He}}^{\text{eff}})^{-\beta} P_{\text{He}}^{2(\beta-\alpha)} t^{\beta-\alpha} \right]^{1/(3\beta-2\alpha)} \quad (15)$$

$$\bar{r}_B \propto (D_{\text{He}}^{\text{eff}} P_{\text{He}} t^2)^{1/(3\beta-2\alpha)} \quad (16)$$

where  $P_{\text{He}}$  is the He production rate,  $t$  is the time for bubble evolution, and  $\alpha, \beta$  are the constants, which depend on the He bubble state. At the scenarios of high temperature and/or low He production rate, the He bubble evolution will be expressed by the multi-atomic nucleation model, which will follow the relationships as [63]:

$$C_B(t \rightarrow \infty) \sim 2C_B^* \propto (P_{\text{He}} / t' c_{\text{He}}^*)^{1/(\gamma+1)} / D_{\text{He}} \quad (17)$$

$$\bar{r}_B(t \rightarrow \infty) \propto \left[ D_{\text{He}} c_{\text{He}}^* {}^{1/(\gamma+1)} (P_{\text{He}} / t')^{\gamma/(\gamma+1)} t^{\gamma+1} \right]^{1/\beta} \quad (18)$$

where  $c_{\text{He}}^*$  is the helium concentration in solution at nucleation peak,  $D_{\text{He}}$  is the He interstitial diffusion coefficient,  $\gamma$  is the constant. Up to now, the two models were successfully utilized to explain the He bubble formation at different irradiation conditions, the He diffusivity is regarded as the main factor for bubble evolution [64,65]. Theoretically, the transition from dual-atomic nucleation to the multi-atomic nucleation will happen when the dissociation rate of a diatomic cluster becomes comparable with the rate of He absorption to it [65]. In this case, the irradiation-produced temperatures (only the thermal spike effect) is low enough while the He production rate is  $\sim 4.58$  appm/s. So, we consider that the dual-atomic nucleation model would most likely happen as compared with the previous studies under the approximate irradiation conditions [22,59].

#### 4.2. Irradiation-induced crystallization mechanisms

As similar to crystallization induced by the thermal annealing in most amorphous or metal glass materials, the energetic ion irradiation-induced crystallization process in amorphous also includes two fundamental courses: nucleation and grain growth. In this case of 60 keV  $\text{He}^+$  irradiated TaTiWCr RHEA and W films, the irradiation-induced crystallization and grain growth can be ascribed to the following stages: (1) the defects accumulation leads to the enhancement of free energy, until the defect concentration reaches a critical level; (2) the irradiation induces a short range diffusion via thermal-spike effect; (3) the entrapment of constituent atoms between the boundaries of amorphous and nano-crystalline regions reduce the GB curvature; (4) the grain growth by GB migration.

These He ions were introduced into the target material to produce abundant vacancy and interstitial defects with increasing fluence, which will boost the free volume and energy deposition, improving the atomic

mobility and rearrangement of atoms in the matrix [41]. The introduced free volume will increase the Gibbs free energy, which would reduce the crystallization activation energy barrier and provide many nucleation sites for crystallization, promoting the formation of nano-meter grains [28,29,41]. More nucleation phenomenons are triggered until the defect concentration reach a critical level, namely, the fluence is higher than  $1 \times 10^{16} \text{ cm}^{-2}$  (0.24 dpa) for the TaTiWCr RHEA, while the fluence is higher than  $1 \times 10^{17} \text{ cm}^{-2}$  (1.27 dpa) for the W in current cases. In addition, most of the defects produced by collision cascade could recombine and annihilate at the boundary between the nano-grains and the amorphous regions, which may serve as a new nucleation for subsequent crystallization [66].

Based on the SRIM simulation results, electronic stopping power and electronic energy deposition of 60 keV  $\text{He}^+$  injected into the RHEA and W leads to a collision cascade owing to the interactions of  $\text{He}^+$  and electron. Subsequently, on account of the discrepancy between electron temperature and lattice temperature, the electronic-excitation energy ( $E_{\text{ionization}}$ ) can be transferred from the hot electron subsystem to the cold lattice subsystem through electron-phonon coupling and subsequently lead to a lattice temperature rise [67]. Once the  $\text{He}^+$  energy deposition exceeds a critical threshold, the irradiation damage produced by energy loss electronic excitation concurrently produce thermal spike effect [67]. The irradiation created vacancy and interstitial present a short range diffusion driven by the thermal-spike effect. It has been reported that vacancies would have to migrate toward GBs and other defect sinks to achieve a new structural and energetic balance in nano-crystalline materials subjected to irradiation environments [41, 66]. An illustration is shown in Fig. 15 (a), the defect annihilation at crystal nucleus can promote the inter-diffusion and exchange between the defect-flux and RHEA or W atoms, finally causing compositional reorganization in RHEA based on an inverse Kirkendall effect (i.e. vacancy or interstitial flux in the opposite direction of net solute flux) [68]. Those diffused metal-atoms are preferentially entrapped by the nano-meter GBs and other defect sinks (bubbles and dislocations), which offer a possibility of grain growth and a new nucleation for subsequent crystallization. Theoretical simulation also disclosed that the amorphous-crystalline boundary dramatically varies with the irradiation time [66]. Hence, there is a tendency that this boundary between the nano-grains and the amorphous matrix will advance towards the amorphous zone, forming abundant spherical or ellipsoidal grains by atomic entrapment (Fig. 15(b)).

Early reports have revealed that the irradiation-induced grain growth was attributed to the thermally assisted grain rotation and curvature-driven mechanisms to reduce the GB curvature [69,70]. As the fluence increase, the grain growth mechanisms are different. At the fluence lower than  $1 \times 10^{17} \text{ cm}^{-2}$ , the original grain present nano-meter sphericity (Fig. 7(c)). Therefore, the driving force for GB migration comes from the curvature of the GB. A curved GB is subject to a pressure i.e., force per unit area of GB of magnitude [70]:

$$P_{\text{curv}} = \frac{2\gamma}{R} \quad (19)$$

where  $\gamma$  is the GB surface energy per unit area,  $R$  is the radius of curvature of the GB, which is equal to the radius of a spherical grain. If the atoms are thermally activated within the thermal spike region near the direct vicinity of GBs, they can easily jump across the boundary. The local driving forces, including chemical concentration gradients and GB curvature, cause the net number of atom jumps to be in the direction of reducing GB curvature [70]. As a result, the GB migrates in the opposite direction, this process is shown in Fig. 15(c). With continuous ion irradiation at high fluence, the fast growth of grains was observed. This is due to the columnar grain structure was induced, and the grains with {110} direction exhibited preferential growth, those nano-grain presented an aggregation and alignment state, as shown in Fig. 15(d). A disorder-driven fast grain growth has revealed by the theoretical

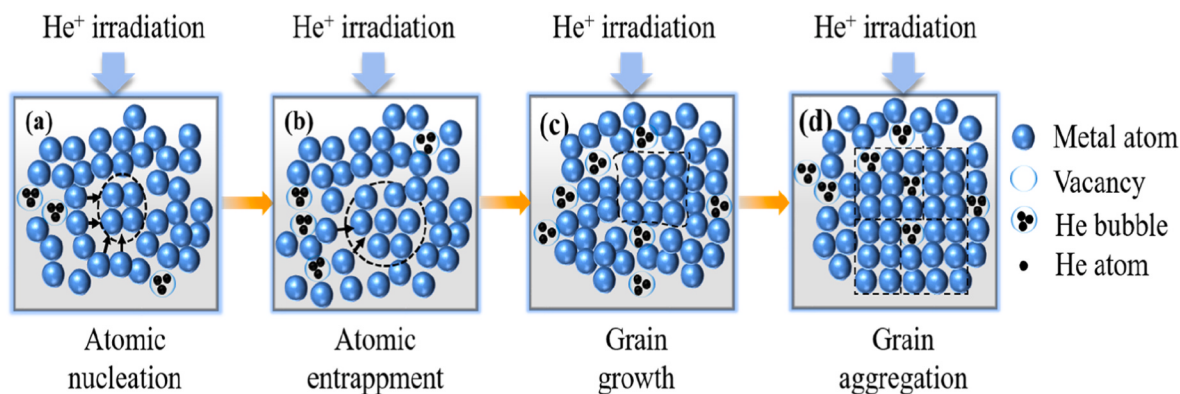


**Fig. 15.** Illustration of irradiation-induced grain growth in TaTiWVCr or W films constructed with amorphous structures.

simulation, this disorder-driven mechanism leads to grain growth on a much shorter time scale (a few tens of picoseconds) as compared to the processes based on curvature-driven or grain-rotation mechanisms (occurring over a few hundreds of picoseconds) [71]. In addition, a mass of point defects (interstitials and vacancies) are produced can be accumulated and absorbed by the GBs, which generate a concentration gradient of defect near the GBs. This concentration difference of defect creates a nonequilibrium environment by atomic collision cascades and provides a driving force to promote grain growth. Under this nonequilibrium environment, the atoms inside one grain will be activated to jump across the GB to an available vacant site of the other grains, resulting in the migration of GB and the subsequent grain growth [72].

#### 4.3. The mechanisms of irradiation-induced swelling

According to the step-height between the irradiated region and the unirradiated region, an integrated swelling was measured directly. By this way, the bubble aggregation produced lattice swelling in the RHEA and W films can reflect the different He behavior during irradiation. At the He fluence less than  $1 \times 10^{17} \text{ cm}^{-2}$ , a low increase tendency in swelling is considered to originate from early nucleation and growth of He-induced bubbles, which is accompanied by an increase in GB density. The nano-meter GBs in the RHEA demonstrate key function in improving swelling resistance by reducing the He bubble sizes, which agrees with the previous result that the abundant GBs serve as effective point defect sinks and reduce swelling by decreasing the vacancy concentration [73]. The irradiation-induced vacancies are prone to occupied by He atoms to form small-sized bubbles, which are further diffused into GBs, reducing the He accumulation and swelling. With an accumulation of He content, the bubble size increases so large that a significant number of bubbles are aggregated in the matrix, resulting in the significant swelling at the fluence of  $2 \times 10^{17} \text{ cm}^{-2}$ . Furthermore, the discrepancy of bubbles distribution and its sizes in the RHEA and W matrix revealed that the RHEA films display higher swelling resistance in comparison with that of W films. Except for the large-sized bubbles in W films, surface blisters contribute to the increased swelling because of its lower implantation depth than that of the RHEA films. The local composition change also affects the swelling behavior. In contrast to the W, less mass migration demonstrates on the surface of RHEA due to its sluggish diffusion. Nevertheless, for the W films, the significant atom migrations near the step-edges increase the integrated swelling.

## 5. Conclusion

In summary, tungsten-containing TaTiWVCr RHEA and metal W films constructed with amorphous structures were irradiated by 60 keV He<sup>+</sup>, the He<sup>+</sup> fluence is ranging from  $1 \times 10^{16} \text{ cm}^{-2}$  to  $2 \times 10^{17} \text{ cm}^{-2}$ . Results showed that the crystallization phenomena in RHEA initially occurred at fluence of  $5 \times 10^{16} \text{ cm}^{-2}$ , and the average grain size

approximate 8.0 nm was obtained at fluence of  $1 \times 10^{17} \text{ cm}^{-2}$ . Meanwhile, the obvious crystallization and maximum grain size of 14.0 nm in pure W films were induced at highest fluence of  $2 \times 10^{17} \text{ cm}^{-2}$ . The results disclosed that the crystallization and grain growth in TaTiWVCr RHEA amorphous films were more easily occurred than the counterpart of W films when exposed to the same He<sup>+</sup> irradiation environment. Those simulation results of electronic stopping power and He<sup>+</sup> energy deposition revealed that the ionized-created energy loss in irradiated regions played critical role in producing inelastic thermal-spikes via electron-phonon coupling, which was responsible for the GB migration and the overall grain growth. At the highest fluence of  $2 \times 10^{17} \text{ cm}^{-2}$ , the phase structure remained stable in RHEA film even though the elements demonstrated local short-range segregation due to the crystallization and the high bubble pressure in RHEA film. In contrast to the W, the smaller-sized bubbles and the less dislocation were demonstrated in the irradiated region of RHEA due to its naturally special high entropy effect and high lattice distortion. Meanwhile, the irradiation-induced blister morphology and the volume swelling between the RHEA and W films were also contrasted by the systematic investigations and revealed the RHEA exhibited more excellent swelling resistance than the counterpart of W films.

#### Credit authorship contribution statement

**Guo Pu:** Conceptualization, Methodology, Investigation, Formal analysis, Writing - original draft, Writing - review & editing. **Sen Sun:** Methodology. **Sishu Wang:** Formal analysis. **Lin Gan:** Writing - review & editing. **Sheng Chen:** Supervision. **Zongbiao Ye:** Writing - review & editing. **Zhangyi Huang:** Investigation. **Jiaochun Zheng:** Investigation. **Zhijun Wang:** Formal analysis. **Chi Yang:** Formal analysis. **Liwei Lin:** Software, Formal analysis, Funding acquisition. **Bo Liu:** Methodology, Funding acquisition. **Kun Zhang:** Methodology, Investigation, Writing - review & editing. **Yihan Wang:** Writing - review & editing, Supervision.

#### Declaration of competing interest

The authors declare that they have no known competing financial interests or personal relationships that could have appeared to influence the work reported in this paper.

#### Data availability

The authors are unable or have chosen not to specify which data has been used.

#### Acknowledgments

This work was supported by NSAF (Grant No. U2130115), the Sichuan Science and Technology Program (Grant NO: 2022YFSY0020)

and the National Key Research and Development Program of China (Grant 2018YFA0702100).

## Appendix A. Supplementary data

Supplementary data to this article can be found online at <https://doi.org/10.1016/j.intermet.2023.107850>.

## References

- [1] M.R. Gilbert, S.L. Dudarev, S. Zheng, L. Packer, J.C. Sublet, An integrated model for materials in a fusion power plant: transmutation, gas production, and helium embrittlement under neutron irradiation, *Nucl. Fusion* 52 (2012), 083019.
- [2] J. Knaster, A. Moeslang, T. Muroga, Materials research for fusion, *Nat. Phys.* 12 (2016) 424.
- [3] Y. Gasparyan, D. Bachurina, V. Efimov, J. Gurova, F. Podolyako, N. Sergeev, I. Sorokin, A. Suchkov, N. Bobyr, I. Kozlov, E. Kulikova, A. Spitsyn, Deuterium retention in the elements of plasma facing components for the DEMO first wall, *J. Nucl. Mater.* 567 (2022), 153837.
- [4] M.R. Gilbert, K. Arakawa, Z. Bergstrom, M.J. Caturla, S.L. Dudarev, et al., Perspectives on multiscale modelling and experiments to accelerate materials development for fusion, *J. Nucl. Mater.* 554 (2021), 153113.
- [5] R. Neu, J. Riesch, J.W. Coenen, J. Brinkmann, A. Calvo, S. Elgeti, C. García-Rosales, H. Greuner, T. Hoeschen, G. Holzner, F. Klein, F. Koch, Ch Linsmeier, A. Litnovsky, T. Wegener, S. Wurster, J.-H. You, Advanced tungsten materials for plasma-facing components of DEMO and fusion power plants, 109–111, *Fusion Eng. Des.* (2016) 1046–1052.
- [6] J.W. Yeh, S.K. Chen, S.J. Lin, J.Y. Gan, Nanostructured high-entropy alloys with multiple principal elements: novel alloy design concepts and outcomes, *Adv. Eng. Mater.* 6 (2004) 299–303.
- [7] G.C. Gruber, A. Lassnig, S. Zak, C. Gammer, M.J. Cordill, R. Franz, Synthesis and structure of refractory high entropy alloy thin films based on the MoNbTaW system, *Surf. Coat. Technol.* 439 (2022), 128446.
- [8] Z. Han, N. Chen, S. Zhao, L. Fan, G. Yang, Y. Shao, K. Yao, Effect of Ti additions on mechanical properties of NbMoTaW and VNbMoTaW refractory high entropy alloys, *Intermetallics* 84 (2017) 153–157.
- [9] W.J. Huang, X.J. Wang, J.W. Qiao, Y.C. Wu, Microstructures and mechanical properties of TiZrHfNbTaWx refractory high entropy alloys, *J. Alloys Compd.* 914 (2022), 165187.
- [10] B.S. Lou, C.J. Wang, Y.Y. Chen, S.B. Hung, Y.C. Lin, J.W. Lee, Phase, mechanical property and corrosion resistance evaluation of W-Nb-Ta-Ti and W-Nb-Ta-Ti-N medium entropy alloy thin films, *Surf. Coat. Technol.* 442 (2022), 128339.
- [11] D. Ikeuchi, D.J.M. King, K.J. Laws, A.J. Knowles, R.D. Aughterson, G.R. Lumpkin, E.G. Obbard, Cr-Mo-V-W, A new refractory and transition metal high-entropy alloy system, *Scripta Mater.* 158 (2019) 141–145.
- [12] Z.D. Han, H.W. Luan, X. Liu, N. Chen, X.Y. Li, Y. Shao, K. Yao, Micro-structures and mechanical properties of TiNbMoTaW refractory high entropy alloys, *Mater. Sci. Eng.* 712 (2018) 380–385.
- [13] M. Wang, Z.L. Ma, Z.Q. Xu, X.W. Cheng, Microstructures and mechanical properties of HfNbTaTiZrW and HfNbTaTiZrMoW refractory high-entropy alloys, *J. Alloys Compd.* 803 (2019) 778–785.
- [14] J.W. Yeh, S.K. Chen, S.J. Lin, J.Y. Gan, Nanostructured high-entropy alloys with multiple principal elements: novel alloy design concepts and outcomes, *Adv. Eng. Mater.* 6 (2004) 299–303.
- [15] N.F. Shkodich, K.V. Kuskov, A.S. Sedegov, A.V. Pantelieeva, Y.S. Vergunova, Yu.B. Scheek, E. Panina, N. Stepanov, I. Serhiienko, D. Moskovskikh, Refractory TaTiNb, TaTiNbZr, and TaTiNbZrX (X = Mo, W) high entropy alloys by combined use of high energy ball milling and spark plasma sintering: structural characterization, mechanical properties, electrical resistivity, and thermal conductivity, *J. Alloys Compd.* 893 (2022), 162030.
- [16] S.K. Bachani, C.J. Wang, B.S. Lou, L.C. Chang, J.W. Lee, Microstructural characterization, mechanical property and corrosion behavior of VNbMoTaW refractory high entropy alloy coatings: effect of Al content, *Surf. Coat. Technol.* 403 (2020), 126351.
- [17] W.R. Zhang, P.K. Liaw, Y. Zhang, A novel low-activation VC<sub>x</sub>FeTaW<sub>x</sub> (x = 0.1, 0.2, 0.3, 0.4, and 1) high-entropy alloys with excellent heat-softening resistance, *Entropy* 20 (2018) 951.
- [18] O.A. Waseem, J. Lee, H.M. Lee, H.J. Ryu, The effect of Ti on the sintering and mechanical properties of refractory high-entropy alloy Ti<sub>x</sub>W<sub>1-x</sub>V<sub>Cr</sub> fabricated via spark plasma sintering for fusion plasma-facing materials, *Mater. Chem. Phys.* 210 (2018) 87–94.
- [19] H.J. Cui, N. Liu, L.M. Luo, Y. Xu, J.G. Cheng, Y.C. Wu, Behavior of high-entropy W-rich alloys W<sub>x</sub>(TaVCrTi)<sub>y</sub> under He<sup>+</sup> irradiation, *Fusion Eng. Des.* 172 (2021), 112904.
- [20] O. El-Atwani, N. Li, M. Li, A. Devaraj, J.K.S. Baldwin, M.M. Schneider, D. Sobieraj, J.S. Wróbel, D. Nguyen-Manh, S.A. Maloy, E. Martinez, Outstanding radiation resistance of tungsten-based high-entropy alloys, *Sci. Adv.* 5 (2019) 1–9.
- [21] D. Patel, M.D. Richardson, B. Jim, S. Akhmadaliev, R. Goodall, A.S. Gandy, Radiation damage tolerance of a novel metastable refractory high entropy alloy V2.5Cr1.2WMoCo0.04, *J. Nucl. Mater.* 531 (2020), 152005.
- [22] G. Pu, L.W. Lin, R. Ang, K. Zhang, B. Liu, B. Liu, T. Peng, S.F. Liu, Q.R. Li, Outstanding radiation tolerance and mechanical behavior in ultra-fine nanocrystalline Al<sub>1.5</sub>CoCrFeNi high entropy alloy films under he ion irradiation, *App. Surf. Sci.* 516 (2020), 146129.
- [23] O. El-Atwani, A. Alvarado, K. Unal, S. Fensin, J.A. Hinks, G. Greaves, J.K. Baldwin, S.A. Maloy, E. Martinez, Helium implantation damage resistance in nanocrystalline W-Ta-V-Cr high entropy alloys, *Mater. Today Energy* 19 (2021), 100599.
- [24] W. Zhang, M. Wang, L. Wang, C.H. Liu, H. Chang, J.J. Yang, J.L. Liao, Y.Y. Yang, N. Liu, Interface stability, mechanical and corrosion properties of AlCrMoNbZr/(AlCrMoNbZr)N high-entropy alloy multilayer coatings under helium ion irradiation, *App. Surf. Sci.* 485 (2019) 108–118.
- [25] G. Pu, Q.R. Li, Y.H. Wang, J. Li, S. Chen, K. Zhang, C. Yang, Z.J. Wang, L.W. Lin, D. Ren, Z.B. Ye, B. Liu, B. Liu, Hierarchical-interface design for stable helium storage and structural evolution in homogeneous nano-multilayered Al<sub>1.5</sub>CoCrFeNi high entropy alloy films, *Surf. Coat. Technol.* 439 (2022), 128393.
- [26] G. Pu, L.W. Lin, D. Ren, K.F. Gan, B. Liu, Z.B. Ye, Y.H. Wang, K. Zhang, Z.M. Li, B. Liu, Influence of tunable interfaces on radiation tolerance and nanomechanical behavior of homogeneous multi-nanolayered Al<sub>1.5</sub>CoCrFeNi high entropy alloy films, *J. Nucl. Mater.* 566 (2022), 153734.
- [27] J. Carter, E.G. Fu, M. Martin, G.Q. Xie, X. Zhang, Y.Q. Wang, D. Wijesundera, X. M. Wang, Ion irradiation induced nanocrystal formation in amorphous Zr55Cu30Al10Ni5 alloy, *Nucl. Instrum. Methods Phys. Res. B* 267 (2009) 2827–2831.
- [28] K. Zhang, Y. Wang, W.H. Zhang, Z. Hu, B.C. Wei, Y.H. Feng, Crystallization behavior and mechanical response of metallic glass induced by ion irradiation at elevated temperature, *J. Nucl. Mater.* 545 (2021), 152618.
- [29] P. Gong, K.F. Yao, H.Y. Ding, Crystallization kinetics of TiZrHfCuNiBe high entropy bulk metallic glass, *Mater. Lett.* 156 (2015) 146–149.
- [30] H.Y. Jing, M.F. Li, P.W. Wang, B. Malomo, L. Yang, Self-healing mechanisms of ZrCu nanocrystalline/amorphous laminated alloy under irradiation, *Materialia* 20 (2021), 101227.
- [31] S.J. Zhao, Defect properties in a VTaCrW equiatomic high entropy alloy (HEA) with the body centered cubic (bcc) structure, *J. Mater. Sci. Technol.* 44 (2020) 133–139.
- [32] Y. Zhang, G.M. Stocks, K. Jin, C. Lu, H. Bei, B.C. Sales, L. Wang, L.K. Beland, R. E. Stoller, G.D. Samolyuk, Influence of chemical disorder on energy dissipation and defect evolution in concentrated solid solution alloys, *Nat. Commun.* 6 (1) (2015) 1–9.
- [33] W.J. Weber, Y.W. Zhang, Predicting damage production in mono-atomic and multi-elemental targets using stopping and range of ions in matter code: challenges and recommendations on the use of SRIM for computing radiation damage exposure, *Solid State Mater. Sci.* 23 (2019), 100757.
- [34] A. E521, Standard practice for neutron radiation damage simulation by charged-particle, *Annu. Book ASTM Stand.* 12 (2009) 1–21.
- [35] G.W. Egeland, J.A. Valdez, S.A. Maloy, K.J. McClellan, K.E. Sickafus, G.M. Bond, Heavy-ion irradiation defect accumulation in ZrN characterized by TEM, GIXRD, nanoindentation, and helium desorption, *J. Nucl. Mater.* 435 (2013) 77–87.
- [36] X. Yang, Y. Zhang, Prediction of high-entropy stabilized solid-solution in multi-component alloys, *Mater. Chem. Phys.* 132 (2012) 233–238.
- [37] B. Vishwanadh, N. Sarkar, S. Gangil, S. Singh, R. Tewari, G.K. Dey, S. Banerjee, Synthesis and microstructural characterization of a novel multicomponent equiatomic ZrNbAlTiV high entropy alloy, *Scripta Mater.* 124 (2016) 146–150.
- [38] P. Sigmund, A. Schinner, Note on measuring electronic stopping of slow ions, *Nucl. Instrum. Methods Phys. Res. B* 410 (2017) 78–88.
- [39] H.H. Andersen, P. Sigmund, Stopping of heavy ions: a topical issue, *Nucl. Instrum. Methods Phys. Res. B* 195 (2002) 1–2.
- [40] Y.W. Zhang, C. Silva, T.G. Lach, M.A. Tunes, Y.F. Zhou, Role of electronic energy loss on defect production and interface stability: comparison between ceramic materials and high-entropy alloys, *Curr. Opin. Solid State Mater. Sci.* 26 (2022), 101001.
- [41] H.Y. Xin, J.J. Yang, W. Zhang, J. Yang, J.J. Mao, C.Q. Teng, X.G. Kong, J.X. Si, X. Y. Xu, W. Zhang, L. Wu, X.Y. Wu, Effect of Au ion irradiation on the surface morphology, microstructure and mechanical properties of AlNbTiZr medium-entropy alloy coatings with various Al content for ATF, *Surf. Coat. Technol.* 434 (2022), 128157.
- [42] W. Zhang, H. Han, J.X. Dai, C.L. Ren, C.B. Wang, L. Yan, H.F. Huang, Z.Y. Zhu, Simulation of migration and coalescence of helium bubbles in nickel, *J. Nucl. Mater.* 518 (2019) 48–53.
- [43] J.S. Lin, L.M. Luo, Q. Xu, X. Zan, X.Y. Zhu, Y.C. Wu, Microstructure and deuterium retention after ion irradiation of W-Lu2O3 composites, *J. Nucl. Mater.* 490 (2017) 272–278.
- [44] X.Y. Tan, L.M. Luo, H.Y. Chen, X.Y. Zhu, X. Zan, G.N. Luo, J.L. Chen, P. Li, J. G. Cheng, D.P. Liu, Y.C. Wu, Mechanical properties and microstructural change of W-Y2O3 alloy under helium irradiation, *Sci. Rep.* 5 (2015), 12755.
- [45] S. Liu, D. Chen, S. Zhao, W. Lin, F. Meng, Y. Zhao, G. Yeli, F. He, Y. Li, H. Niu, J. jung Kai, Temperature-dependent helium induced microstructural evolution in equiatomic NiCo and NiFe concentrated solid solution alloys, *J. Nucl. Mater.* 545 (2021), 152715.
- [46] Y. Zhang, X. Wang, Y.N. Osetsky, Y. Tong, R. Harrison, S.E. Donnelly, D. Chen, Y. Wang, H. Bei, B.C. Sales, K.L. More, P. Xiu, L. Wang, W.J. Weber, Effects of 3d electron configurations on helium bubble formation and void swelling in concentrated solid-solution alloys, *Acta Mater.* 181 (2019) 519–529.
- [47] Z.X. Shang, J. Ding, C.C. Fan, D. Chen, J. Li, Y.F. Zhang, Y.Q. Wang, H.Y. Wang, X. H. Zhang, He ion irradiation response of a gradient T91 steel, *Acta Mater.* 196 (2020) 175–190.
- [48] W.R. Tyson, W.A. Miller, Surface free energies of solid metals: estimation from liquid surface tension measurements, *Surf. Sci.* 62 (1977) 267–276.

- [49] X.J. Yao, X.F. Shi, Y.P. Wang, G.Y. Gan, B.Y. Tang, The mechanical properties of high entropy (-like) alloy W<sub>x</sub>(TaTiVCr)<sub>1-x</sub> via first-principles calculations, *Fusion Eng. Des.* 137 (2018) 35–42.
- [50] H. Schroeder, F.P.F. Paulo, On the coarsening mechanisms of helium bubbles Ostwald ripening versus migration and coalescence, *J. Nucl. Mater.* (1991) 179–181, 1007–1010.
- [51] I.R. Brearley, D.A. MacInnes, An improved equation of state for inert gases at high pressures, *J. Nucl. Mater.* 95 (1980) 239–252.
- [52] W.T. Lin, G.M. Yeli, G. Wang, J.H. Lin, S.J. Zhao, D. Chen, S.F. Liu, F.L. Meng, Y. R. Li, F. He, Y. Lu, J.J. Kai, He-enhanced heterogeneity of radiation-induced segregation in FeNiCoCr high-entropy alloy, *J. Mater. Sci. Technol.* 101 (2022) 226–233.
- [53] D. Li, N. Jia, H. Huang, S. Chen, Y. Dou, X. He, W. Yang, Y. Xue, Z. Hua, F. Zhang, L. Wang, K. Jina, H. Cai, Helium ion irradiation enhanced precipitation and the impact on cavity formation in a HfNbZrTi refractory high entropy alloy, *J. Nucl. Mater.* 552 (2021), 153023.
- [54] W.Y. Chen, J.D. Poplawsky, Y. Chen, W. Guo, J.W. Yeh, Irradiation-induced segregation at dislocation loops in CoCrFeMnNi high entropy alloy, *Materialia* 14 (2020), 100951.
- [55] T. Nagase, P.D. Rack, J.H. Noh, T. Egami, In-situ TEM observation of structural changes in nano-crystalline CoCrCuFeNi multicomponent high-entropy alloy (HEA) under fast electron irradiation by high voltage electron microscopy (HVEM), *Intermetallics* 59 (2015) 32–42.
- [56] S.Q. Xia, X. Yang, T.F. Yang, S. Liu, Y. Zhang, Irradiation resistance in Al<sub>x</sub>CoCrFeNi high entropy alloys, *J. Occup. Med.* 67 (2015) 2340–2344.
- [57] S.L. Shang, B.C. Zhou, W.Y. Wang, A.J. Ross, X.L. Liu, Y.J. Hu, H.Z. Fang, Y. Wang, Z.K. Liu, A comprehensive first-principles study of pure elements: vacancy formation and migration energies and self-diffusion coefficients, *Acta Mater.* 109 (2016) 128–141.
- [58] S.W. McAlpine, Materials Design for Advanced Nuclear Energy Systems: Refractory High Entropy Alloys and Metallic Multilayer Composites, 2022.
- [59] D. Chen, S.J. Zhao, J.R. Sun, P.F. Tai, Y.B. Sheng, Y.L. Zhao, G. Yeli, W.T. Lin, S. F. Liu, W. Kai, J.J. Kai, Diffusion controlled helium bubble formation resistance of FeCoNiCr high-entropy alloy in the half-melting temperature regime, *J. Nucl. Mater.* 526 (2019), 151747.
- [60] S. Zhao, T. Egami, G.M. Stocks, Y. Zhang, Effect of d electrons on defect properties in equiatomic NiCoCr and NiCoFeCr concentrated solid solution alloys, *Phys. Rev. Mater.* 2 (2018).
- [61] H. Trinkaus, B.N. Singh, Helium accumulation in metals during irradiation—where do we stand? *J. Nucl. Mater.* 323 (2–3) (2003) 229–242.
- [62] G.S. Was, Fundamentals of Radiation Materials Science: Metals and Alloys, Springer, 2016.
- [63] H. Trinkaus, Modeling of helium effects in metals: high temperature embrittlement, *J. Nucl. Mater.* 133 (1985) 105–112.
- [64] C. Zhang, K. Chen, Y. Wang, J. Sun, D. Shen, Formation of bubbles in helium implanted 316L stainless steel at temperatures between 25 and 550°C, *J. Nucl. Mater.* 245 (1997) 210–216.
- [65] B. Singh, H. Trinkaus, An analysis of the bubble formation behaviour under different experimental conditions, *J. Nucl. Mater.* 186 (2) (1992) 153–165.
- [66] F. Xiong, M.F. Li, B. Malomo, L. Yang, Microstructural evolution in amorphous-nanocrystalline ZrCu alloy under neutron irradiation, *Acta Mater.* 182 (2020) 18–28.
- [67] Y. Liu, Q. Huang, H.Z. Xue, M.L. Crespiello, P. Liu, X.L. Wang, Thermal spike response and irradiation-damage evolution of a defective YAlO<sub>3</sub> crystal to electronic excitation, *J. Nucl. Mater.* 499 (2018) 312–316.
- [68] A.D. Marwick, Segregation in irradiated alloys: inverse kirkendall effect and effect of constitution on void swelling, *J. Phys. F Met. Phys.* 8 (1978) 1849–1861.
- [69] W. Voegeli, K. Albe, H. Hahn, Simulation of grain growth in nanocrystalline nickel induced by ion irradiation, *Nucl. Instrum. Methods Phys. Res., Sect. B* 202 (2003) 230–235.
- [70] D. Kaoumi, , 1 A.T. Motta,1, R.C. Birtcher, A thermal spike model of grain growth under irradiation, *J. Appl. Phys.* 104 (2008), 073525.
- [71] Y.W. Zhang, D.S. Aidhy, T. Varga, S. Moll, P.D. Edmondson, F. Namavar, K. Jin, C. N. Ostrouchov, W.J. Weber, The effect of electronic energy loss on irradiation-induced grain growth in nanocrystalline oxides, *Phys. Chem. Chem. Phys.* 16 (2014) 8051.
- [72] J.R. Zhou, M. Islam, S.M. Guo, Y. Zhang, F.Y. Lu, Radiation-induced grain growth of nanocrystalline Al<sub>x</sub>CoCrFeNi high-entropy alloys, *J. Phys. Chem. C* 125 (2021) 3509–3516.
- [73] G. Ayrault, Cavity formation during single- and dual-ion irradiation in a 9Cr-1Mo ferritic alloy, *J. Nucl. Mater.* 114 (1983) 34–40.